

Gravitational wave transient signal emission via Ekman pumping in neutron stars during post-glitch relaxation phase

Avneet Singh*

*Max-Planck-Institut für Gravitationsphysik, am Mühlenberg 1, 14476 Potsdam-Golm, Germany;**Max-Planck-Institut für Gravitationsphysik, Callinstraße 38, 30167 Hannover, Germany**and Leibniz Universität Hannover, Welfengarten 1, 30167 Hannover, Germany*

(Received 30 May 2016; published 20 January 2017)

Glitches in the rotational frequency of a spinning neutron star could be promising sources of gravitational wave signals lasting between a few microseconds to a few weeks. The emitted signals and their properties depend upon the internal properties of the neutron star. In neutron stars, the most important physical properties of the fluid core are the viscosity of the fluid, the stratification of flow in the equilibrium state, and the adiabatic sound speed. Such models were previously studied [C. A. van Eysden and A. Melatos, *Classical Quantum Gravity* **25**, 225020 (2008); M. F. Bennett, C. A. van Eysden, and A. Melatos, *Mon. Not. R. Astron. Soc.* **409**, 1705 (2010)] following simple assumptions on all contributing factors, in which the post-glitch relaxation phase could be driven by the well-known process of *Ekman pumping* [G. Walin, *J. Fluid Mech.* **36**, 289 (1969); M. Abney and R. I. Epstein, *J. Fluid Mech.* **312**, 327 (1996)]. We explore the hydrodynamic properties of the flow of fluid during this phase following more relaxed assumptions on the stratification of flow and the pressure-density gradients within the neutron star than previously studied. We calculate the time scales of duration as well as the amplitudes of the resulting gravitational wave signals, and we detail their dependence on the physical properties of the fluid core. We find that it is possible for the neutron star to emit gravitational wave signals in a wide range of decay time scales and within the detection sensitivity of aLIGO for selected domains of physical parameters.

DOI: 10.1103/PhysRevD.95.024022

I. INTRODUCTION

Pulsar glitches are sudden fractional increases in the rotational velocity of a neutron star. Several pulsars, observed in radio, x-ray, and γ -ray bands of the electromagnetic spectrum, have been repeatedly observed to glitch [1–3]. The fractional spin-up $\delta\Omega$ of the rotational velocity Ω of the neutron star lies in the range of $\frac{\delta\Omega}{\Omega} \in [O(10^{-11}), O(10^{-4})]$ [2,4,5].

Gravitational wave emission is typically associated with a nonzero derivative of the quadrupole moment stemming from the accelerated flow of the nonaxisymmetrically distributed bulk of matter. It is possible that such nonaxisymmetric motions are excited following a glitch; possible mechanisms for producing such nonaxisymmetric motions, besides *Ekman pumping*, include bulk two-stream instabilities [6], surface two-stream instabilities [7], crust deformation and precession [8], meridional circulation and superfluid turbulence driven by crust-core differential rotation [9], crust-core coupling via the magnetic field [10], excitation of pulsation modes [11–13], and mutual friction in a two-fluid model for the superfluid core [14]. These mechanisms were briefly reviewed by van Eysden and Melatos [5] and Bennett *et al.* [15]. In this paper, we solely consider the hydrodynamic properties of the fluid

core following a glitch and concentrate on the mechanism of Ekman pumping.

In this work, we consider the hydrodynamic evolution of the post-glitch relaxation phase via the mechanism of Ekman pumping, pioneered by Walin [16] and Abney and Epstein [17]. We extend the previous works on this by van Eysden and Melatos [5] and Bennett *et al.* [15], where an initial nonaxisymmetric perturbation introduced by the glitch induces Ekman pumping in the core of the star. Ekman pumping is briefly described as the induced flow of the bulk matter in the core when it is acted upon by a tangential force (in this case, Coriolis force) at its boundary, i.e., the crust-core interface. In our case, the Coriolis force results from the differential rotation of the crust with respect to the bulk fluid, resulting from the glitch in the star's rotational velocity. This induced flow of the bulk matter could then have a time-varying quadrupole moment and led to the emission of gravitational waves. In this context, a glitch can lead to gravitational wave emission in two phases. Initially, a burst-type emission occurs during the fast spin-up of crust at time scales of, at most, a few seconds [18]. Second, a decaying continuous-wave signal during the post-glitch relaxation phase is emitted on much longer time scales. The initial nonaxisymmetric motion of the bulk with respect to the crust in the second case is excited by the glitch. The resulting damped continuous-wave-like signal arises as the internal fluid dynamics evolve to set the bulk in corotation or a steady differential

*avneet.singh@aei.mpg.de, avneet.singh@ligo.org

rotation with the crust, erasing the nonaxisymmetric motions in the bulk [5,15].

In this paper, we relax certain assumptions in more recent works [5,15] on the stratification length and the adiabatic sound speed; we explore a regime of Ekman pumping where these quantities are allowed to vary across the star and study their effect on the emitted gravitational wave signal. This extends the parameter space and introduces more generality to the analysis.

We will keep other simplifying assumptions made in [5,17] and analyze the system in a pure hydrodynamical sense, ignoring the two-stream dynamics, sidestepping the crust-core interface, neglecting the effects of the pinning and unpinning of quantum vortices, disallowing the crust to precess, and ignoring the affects of the magnetic field. Specifically, the inclusion of a magnetic field in the current model would make it analytically intractable. In the spirit of first tackling these two aspects separately, i.e., the magnetic field and Ekman pumping, this paper concentrates on the latter process only; such an approach has been extensively considered in the past [5,15,17]. Moreover, for analytic simplicity, we approximate our spherical neutron star to a fluid-filled rigid cylinder [15], as opposed to the choice of semirigidity [5]. The correctness of this choice will be explained in the next section. In a nutshell, as a result of all of these simplifications, a toy model for a neutron star is studied for the possibility of the emission of gravitational waves.

II. HYDRODYNAMICS OF THE SYSTEM

Let us consider a rotating neutron star of a radius of order $O(L)$ with a solid crust around a compressible and viscous fluid with viscosity ν , pressure p , and density ρ . We approximate this spherical system with a rigid cylindrical container of height $2L$ and radius L rotating at an angular

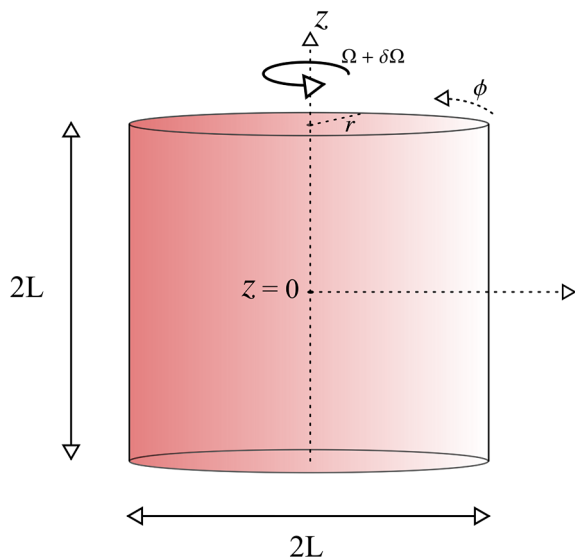


FIG. 1. The idealized system.

frequency of Ω along the z axis (Fig. 1). We represent the glitch as a sudden perturbation in the angular velocity of magnitude $\delta\Omega$ along the z axis. This geometric simplification does not lead to an order-of-magnitude change in the amplitude or duration of the emitted gravitational wave signal from Ekman pumping [19], and it has been extensively used in the literature for neutron star modeling. Moreover, this reformulation to the cylindrical system leads to simpler analytic solutions.

A. Governing equations

Our physical system is described by the velocity field \vec{v} , the pressure p , and the density ρ of the fluid. The forces acting on fluid elements of the bulk volume are the viscous force, the Coriolis force, the centrifugal force, the compressible strain, pressure gradients, and the gravitational force. The Navier-Stokes equation, the conservation of mass equation, and the “energy equation” (i.e., the equation of state) govern our physical system. The Navier-Stokes equation for a fluid element in the rotating Lagrangian frame of the cylinder for a compressible fluid is given as

$$\frac{\partial \vec{v}}{\partial t} + \vec{v} \cdot \nabla \vec{v} + 2\vec{\Omega} \times \vec{v} = -\frac{1}{\rho} \nabla p + \nu \nabla^2 \vec{v} + \frac{\nu}{3} \nabla(\nabla \cdot \vec{v}) + \nabla[\Omega \times (\Omega \times r)] + \vec{g}, \quad (1)$$

where \vec{v} is the fluid velocity and \vec{g} is the gravitational acceleration. The Navier-Stokes equation relates the restoring forces on a fluid element (written on the right-hand side: pressure gradients, viscous force, gravitational force, compressible strain, centrifugal force) to the impulsive change in momentum of the fluid element (written on the left-hand side: Coriolis force, etc.). We have ignored terms from the magnetic field of the neutron star, as previously stated, restricting ourselves to a purely hydrodynamic analysis. The gravitational acceleration is taken to be of the following form:

$$\vec{g} = -\frac{z}{|z|} g \hat{z}. \quad (2)$$

This form for \vec{g} is unphysical since it is generated by a singular and planar mass distribution located at $z = 0$. However, such a choice is standard in the neutron star literature [5,17]; it is equivalent to a radial field for a sphere, which compares well to numerical simulations comprising more realistic mass distributions [20]. This assumption leads to symmetric flow across the midplane of the cylinder and we can restrict ourselves to $z \geq 0$.

The second governing equation is the “continuity equation,” i.e., the conservation of mass equation

$$\frac{\partial \rho}{\partial t} + \nabla \cdot (\rho \vec{v}) = 0. \quad (3)$$

Last, we write the energy equation—i.e., the equation of state—in terms of the adiabatic sound speed v_c (where the subscript S represents the derivative taken at constant entropy) of the form

$$\left[\frac{\partial p}{\partial \rho}\right]_S = v_c^2, \quad (4)$$

which, in the adiabatic limit.¹ and expressed in the Lagrangian frame, takes the following form:

$$\left[\frac{\partial}{\partial t} + \vec{v} \cdot \nabla\right] \rho = \left[\frac{\partial}{\partial t} + \vec{v} \cdot \nabla\right] \frac{p}{v_c^2}. \quad (5)$$

Note that we do not impose invariance of v_c in either space or time, as was previously done in [5,15].

In addition, we scale our variables to dimensionless form by redefining them as $r \rightarrow Lr$, $z \rightarrow Lz$, $\vec{v} \rightarrow (\delta\Omega)L\vec{v}$, $\rho \rightarrow \rho_0\rho$, $p \rightarrow \rho_0gLp$, $\nabla \rightarrow L^{-1}\nabla$, $t \rightarrow t_e t$, where we define ρ_0 as the equilibrium mass density at $z = 0$, and t_e and the Ekman number E as

$$t_e = E^{\frac{1}{2}}\Omega^{-1}, \quad \text{and}, \quad E = \frac{\nu}{L^2\Omega}. \quad (6)$$

One can then write the governing equations (1), (3), and (5) in the rescaled form as

$$\begin{aligned} \epsilon F \left[E^{\frac{1}{2}} \frac{\partial \vec{v}}{\partial t} + \epsilon \vec{v} \cdot \nabla \vec{v} + 2\hat{e}_z \times \vec{v} \right] \\ = -\frac{1}{\rho} \nabla p - \vec{e}_z + \epsilon F E \left[\nabla^2 \vec{v} + \frac{1}{3} \nabla \{ \nabla \cdot \vec{v} \} \right] + F \nabla \left[\frac{1}{2} r^2 \right], \end{aligned} \quad (7)$$

$$E^{\frac{1}{2}} \frac{\partial \rho}{\partial t} + \epsilon \nabla \cdot (\rho \vec{v}) = 0, \quad (8)$$

$$E^{\frac{1}{2}} \frac{\partial [\rho \eta]}{\partial t} + \epsilon \vec{v} \cdot \nabla [\rho \eta] = K \left[E^{\frac{1}{2}} \frac{\partial p}{\partial t} + \epsilon \vec{v} \cdot \nabla p \right], \quad (9)$$

where η , the *Froude number* F, the maximum *scaled compressibility* K, and ϵ are defined as

$$\eta = \frac{v_c^2}{c^2}, \quad K = g \frac{L}{c^2}, \quad F = \Omega^2 \frac{L}{g}, \quad \epsilon = \frac{\delta\Omega}{\Omega}. \quad (10)$$

B. Orders of magnitude

Here, we list the physical constants and parameters introduced in the previous section, and their order-of-magnitude values in SI units for the interior of a neutron star from estimates on the expected and observed physical properties:

¹The adiabatic limit for an isolated neutron star allows us to drop the subscript S in (4); see Sec. VIC for further discussion.

$$\begin{aligned} g = O(10^{12}), \quad L = O(10^4), \quad \frac{\Omega}{2\pi} = O(1 \text{ Hz} - 10^2 \text{ Hz}), \\ E \in [O(10^{-17}), O(10^{-7})], \quad \frac{v_c}{c} \in [O(10^{-2}), 1]. \end{aligned} \quad (11)$$

The viscosity ν of the fluid for a neutron star is currently unknown and widely debated. The associated value of Ekman number E also remains volatile. Yet, there are estimates on the value of E from results of heavy-ion collision experiments [5,21–24] and from theoretical calculations of neutron-neutron scattering in the superfluid limit [25,26]. The results from such an analysis lead to the wide range of possible values for E quoted above in (11). The parameters listed in (10) then take the following values²:

$$\begin{aligned} K = O(10^{-1}), \quad F \in [O(10^{-9}), O(10^{-3})], \\ \epsilon \in [O(10^{-11}), O(10^{-4})]. \end{aligned} \quad (12)$$

III. SOLUTION

In this section, we solve the governing equations given in Sec. II A.

A. Equilibrium solution

In equilibrium, because of the symmetry of the system across the $z = 0$ midplane, the flow is steady and axisymmetric, and the density and pressure are functions of z and r only. Since ϵ and F are quite small in their absolute magnitude, we can ignore the centrifugal term [17] in the rescaled equations (7), (8), and (9). With this approximation, (7) reduces to

$$\frac{1}{\rho} \nabla p + \vec{e}_z = 0. \quad (13)$$

In order to solve the above equation, we need to make an assumption for either the mass density or the pressure. We introduce the dimensionless parameter K_s , following [5], and assume the following:

$$\rho^{-1} (d\rho/dz) = -K_s(z). \quad (14)$$

The stratification length, z_s , is defined in terms of the dimensionless quantity K_s as $z_s = LK_s^{-1}$. The above expression defines a steady-state density profile of the system. The equilibrium pressure and density profiles are then given by solving (13) and (14), respectively, as

$$\rho_e(z) = e^{-\int_0^z K_s(z') dz'}, \quad (15)$$

²We will use the values quoted in (11) and (12) when making order-of-magnitude estimates on the emitted gravitational wave signals.

$$p_e(z) = K_s^{-1}(z) e^{-\int_0^z K_s(z') dz'}. \quad (16)$$

Here, we have not assumed K_s to be a constant, as was done in [5,15]. The introduction of the form K_s is not trivial. In fact, the assumption of a certain form of K_s incorporates the nature of entropic or compositional gradients, which, in turn, incorporate the deviation of an equilibrium state from an adiabatic state. We introduce *equilibrium sound speed* accordingly, given as $v_{\text{eq}}^2 = \frac{gL}{K_s(z)}$. We note that, in the equilibrium state, gravity acts to vary the density and pressure along the axis of the cylinder.

B. Induced perturbations

Let us assume that a glitch induces perturbations in pressure, density, and velocity fields of the internal bulk fluid of the neutron star, and that the resultant bulk fluid flow may be nonaxisymmetric. When such nonaxisymmetric perturbations are induced, the density $\rho(r, \phi, z, t)$ and pressure $p(r, \phi, z, t)$ are functions of all spatial coordinates and time, as opposed to the case of stable equilibrium. In order to solve for the perturbed fluid motion, we treat the system “perturbatively,” given the small magnitude of ϵ . In the perturbative treatment, the density, the pressure, and the velocity field can be expanded as $\rho \rightarrow \rho + \epsilon \delta\rho$ and $p \rightarrow p + \epsilon \delta p$, where we have let the magnitude of δp and $\delta\rho$ run free and have normalized it by ϵ . The perturbed velocity field, however, is written simply as $\vec{v} \rightarrow \delta\vec{v}$. We do not perturb η explicitly; the variation in η comes naturally from the variation in v_c . Now, ignoring all terms larger than $O(1)$ in ϵ , the set of three rescaled governing equations, (7), (8), and (9), reduce to

$$\begin{aligned} & \text{F} \left[E^{\frac{1}{2}} \frac{\partial[\delta\vec{v}]}{\partial t} + 2\hat{e}_z \times [\delta\vec{v}] \right] \\ &= -\frac{1}{\rho} \nabla[\delta p] - \frac{\delta\rho}{\rho} \hat{e}_z + \text{FE} \left[\nabla^2[\delta\vec{v}] + \frac{1}{3} \nabla\{\nabla \cdot [\delta\vec{v}]\} \right] \\ &+ \text{F} \frac{\delta\rho}{\rho} \nabla \left[\frac{1}{2} r^2 \right], \end{aligned} \quad (17)$$

$$E^{\frac{1}{2}} \frac{\partial[\delta\rho]}{\partial t} + \nabla \cdot (\rho \delta\vec{v}) = 0, \quad (18)$$

$$E^{\frac{1}{2}} \frac{\partial[\eta \delta\rho]}{\partial t} + \delta\vec{v} \cdot \nabla[\rho\eta] = \text{K} \left[E^{\frac{1}{2}} \frac{\partial[\delta\rho]}{\partial t} + \delta\vec{v} \cdot \nabla p \right]. \quad (19)$$

C. Method of multiple scales

In the perturbative treatment, we employ the *method of multiple scales* [5,15–17]. The perturbations in the density, pressure, and velocity field are expanded into scales of order E^0 , $E^{\frac{1}{2}}$, and E^1 , such that, for density perturbations,

$$\delta\rho = \delta\rho^{(0)} + E^{\frac{1}{2}} \delta\rho^{(1)} + E^1 \delta\rho^{(2)}, \quad (20)$$

and for pressure perturbations,

$$\delta p = \delta p^{(0)} + E^{\frac{1}{2}} \delta p^{(1)} + E^1 \delta p^{(2)}, \quad (21)$$

and for velocity perturbations,

$$\delta\vec{v} = \delta\vec{v}^{(0)} + E^{\frac{1}{2}} \delta\vec{v}^{(1)} + E^1 \delta\vec{v}^{(2)}. \quad (22)$$

The idea behind the method of multiple scales is to separate subprocesses that occur at time scales in increments of $E^{\frac{1}{2}}$, and to solve them individually.

One can now solve (17) for the velocity field, its radial, azimuthal, and vertical components of $v_r^{(i)}$, $v_\phi^{(i)}$, and $v_z^{(i)}$, up to i th order in $E^{\frac{1}{2}}$,

$$\begin{aligned} \text{F} \left[E^{\frac{1}{2}} \frac{\partial \delta v_r}{\partial t} - 2\delta v_\phi \right] &= -\frac{\partial}{\partial r} \left[\frac{\delta p}{\rho} \right] + \text{FE} \times \left[\left\{ \nabla^2 - \frac{1}{r^2} \right\} \delta v_r \right. \\ &\quad \left. - \frac{2}{r^2} \frac{\partial[\delta v_\phi]}{\partial \phi} + \frac{1}{3} \frac{\partial}{\partial r} [\nabla \cdot \delta\vec{v}] \right], \end{aligned} \quad (23)$$

$$\begin{aligned} \text{F} \left[E^{\frac{1}{2}} \frac{\partial \delta v_\phi}{\partial t} - 2\delta v_r \right] &= -\frac{1}{r} \frac{\partial}{\partial \phi} \left[\frac{\delta p}{\rho} \right] + \text{FE} \times \left[\left\{ \nabla^2 - \frac{1}{r^2} \right\} \delta v_\phi \right. \\ &\quad \left. - \frac{2}{r^2} \frac{\partial[\delta v_r]}{\partial \phi} + \frac{1}{3r} \frac{\partial}{\partial \phi} [\nabla \cdot \delta\vec{v}] \right], \end{aligned} \quad (24)$$

$$\begin{aligned} \text{FE}^{\frac{1}{2}} \frac{\partial \delta v_z}{\partial t} &= -\frac{1}{\rho} \frac{\partial}{\partial z} \left[\frac{\delta p}{\rho} \right] - \frac{\delta\rho}{\rho} + \text{FE} \\ &\times \left[\nabla^2[\delta v_z] - \frac{1}{3} \frac{\partial}{\partial \phi} [\nabla \cdot \delta\vec{v}] \right]. \end{aligned} \quad (25)$$

Two additional relations are derived from the energy equation (19) and the continuity equation (18), and they are given as

$$E^{\frac{1}{2}} \frac{\partial}{\partial t} \left[\frac{\delta\rho}{\rho} \right] + \nabla \cdot \delta\vec{v} = K_s(z) \delta v_z, \quad (26)$$

and

$$\eta(z) E^{\frac{1}{2}} \frac{\partial}{\partial t} \left[\frac{\delta\rho}{\rho} \right] = \text{KE}^{\frac{1}{2}} \frac{\partial}{\partial t} \left[\frac{\delta p}{\rho} \right] + \text{FN}^2(z) \delta v_z, \quad (27)$$

where we have introduced $N(z)$ —the redefined *Brunt-Väisälä frequency*,³

³Note that the Brunt-Väisälä frequency N is a well-known quantity in fluid mechanics and atmospheric sciences. It is a measure of the buoyant force experienced by a fluid element when displaced from equilibrium.

$$N^2(z) = \frac{[\eta K_s - \partial_z \eta] - K}{F} = \frac{K}{F} \left[\frac{v_c^2}{v_{\text{eq}}^2} - 1 \right] - \frac{\partial_z \eta}{F}. \quad (28)$$

We can reformulate (28) by introducing $K'_s(z)$ as

$$K'_s(z) = \eta K_s - \partial_z \eta = K \frac{v_c^2}{v_{\text{eq}}^2} - \partial_z \eta, \quad (29)$$

such that (28) takes the form

$$N^2(z) = \frac{K'_s(z) - K}{F}. \quad (30)$$

Here, η and K_s are allowed to vary with z only. In the set of equations (23)–(27), the terms on different $O(E^0)$, $O(E^{\frac{1}{2}})$, and $O(E^1)$ scales are reducible at each order. Moreover, we can distinguish and deduce the time scales at which several processes contribute to the overall perturbed flow of the bulk matter, such as the formation of a viscous *Rayleigh shear layer*, followed by partial spin-up of the interior fluid via Ekman pumping, followed by complete spin-up of the interior on longer time scales. These processes have been discussed briefly by van Eysden and Melatos [5] and in much greater detail by Abney and Epstein [17]. We will also discuss them in later sections. These time scales are $E^0 \Omega^{-1}$, $E^{-\frac{1}{2}} \Omega^{-1}$, and $E^{-1} \Omega^{-1}$. One can now isolate solutions at these different scales since they are effectively independent due to the very small magnitude of the *Ekman number* E .

D. $O(E^0)$ solutions

On the order of E^0 , expressions (23)–(27) yield

$$\delta v_r^{(0)} = -\frac{1}{2Fr} \frac{\partial}{\partial \phi} \left[\frac{\delta p^{(0)}}{\rho} \right], \quad (31)$$

$$\delta v_\phi^{(0)} = \frac{1}{2F} \frac{\partial}{\partial r} \left[\frac{\delta p^{(0)}}{\rho} \right], \quad (32)$$

$$\delta v_z^{(0)} = 0, \quad (33)$$

$$\delta \rho^{(0)} = -\frac{\partial [\delta p^{(0)}]}{\partial z}, \quad \text{and} \quad (34)$$

$$\nabla \cdot \delta \vec{v}^{(0)} = 0. \quad (35)$$

Note that the solutions on the order E^0 are exactly the same as those previously achieved in [5,15–17]. These solutions, given by (31)–(35), correspond to the formation of a viscous boundary layer (also referred to as the *Rayleigh shear layer*) on the top and bottom faces of the cylinder on a time scale $O(E^0 \Omega^{-1})$. Within this viscous boundary layer, the flow moves radially outward due to the gradient in the

azimuthal velocity and the resulting imbalance between the centrifugal and pressure gradient forces [16,17].

E. $O(E^{\frac{1}{2}})$ solutions

In solving for the $O(E^{\frac{1}{2}})$ solutions, we assume that

$$\frac{\delta p^{(0)}}{\rho} \gg \frac{\delta p^{(1)}}{\rho} \sim 0, \quad \frac{\delta \rho^{(0)}}{\rho} \gg \frac{\delta \rho^{(1)}}{\rho} \sim 0. \quad (36)$$

The $O(E^{\frac{1}{2}})$ terms in (23)–(27) yield

$$\delta v_r^{(1)} = \frac{1}{4F} \frac{\partial \chi}{\partial r}, \quad (37)$$

$$\delta v_\phi^{(1)} = \frac{1}{4Fr} \frac{\partial \chi}{\partial \phi}, \quad (38)$$

$$\delta v_z^{(1)} = \frac{\eta(z)}{FN^2(z)} \frac{\partial \chi}{\partial z} + \left[\frac{-\partial_z \eta}{FN^2(z)} - 1 \right] \chi, \quad \text{and} \quad (39)$$

$$\frac{\partial}{\partial t} \left[\frac{\delta \rho^{(0)}}{\rho} \right] + \nabla \cdot \delta \vec{v}^{(1)} = K_s(z) \delta v_z^{(1)}, \quad (40)$$

where we have defined χ as

$$\chi = -\frac{\partial}{\partial t} \left[\frac{\delta p^{(0)}}{\rho} \right] \sim O(E^0). \quad (41)$$

This set of solutions represents the process of Ekman pumping—the flow in the viscous boundary layer, given by (31)–(35), sets a secondary motion in the interior,⁴ by which the fluid is pulled into the viscous boundary layer from the interior to replace the radial outward flow in it [16,17]. Note that the results on the order $O(E^{\frac{1}{2}})$, given by (37)–(40), are different from those in previous works with respect to the expression for $\delta v_z^{(1)}$ (39) and the continuity equation (40). This affects all future calculations and results.

F. More on the scale-based solutions

We will skip the discussion of the $O(E^1)$ solutions since they occur on much larger time scales of $O(E^{-1} \Omega^{-1})$. These $O(E^{-1} \Omega^{-1})$ solutions correspond to the eventual “spin-up” of the entire interior bulk matter when the interior bulk sets in complete corotation or steady differential corotation with the crust, as previously mentioned [16,17]. This subprocess on much larger time scales is irrelevant to our discussion since it does not contribute to the gravitational wave emission. To recap the scale-based solutions, the sudden spin-up of the rotating cylinder leads to the formation of a

⁴The important development is the excitation of flow in the z direction in the boundary layer, given by (39).

viscous boundary layer at the top and bottom faces of the rotating cylinder. This viscous layer forms on a time scale of $O(E^0\Omega^{-1})$. The velocity field within this layer pushes the fluid radially outward across the layer, given by (31)–(33). The $O(E^0)$ flow excites Ekman pumping in the interior on a time scale of $O(E^{-\frac{1}{2}}\Omega^{-1})$, pushing the fluid radially inward and vertically into the boundary layer, given by (37)–(39). Note that the vertical velocity of the $O(E^{-\frac{1}{2}})$ flow, given by (39), is nonzero. This vertical velocity is constrained by the continuity law applied to the viscous layer [5,15–17], such that

$$\delta v_z|_{z=\pm 1} = \pm \frac{1}{2} E^{\frac{1}{2}} [\nabla \times (\delta \vec{v} - \vec{v}_B)]_z|_{z=\pm 1}, \quad (42)$$

where \vec{v}_B is the dimensionless velocity of the boundary layer in the frame rotating at Ω . In this rotating frame, $\vec{v}_B = r\vec{e}_\phi$ [15]. Note that we have assumed that the boundary layer is rigidly corotating with the cylinder with angular frequency $\Omega + \delta\Omega$ without any slippage. The above expression (42) describes the continuity of the vertical flow across and inside the viscous boundary layer as a function of flow just outside the layer. This process occurs on a time scale of $O(E^{\frac{1}{2}})$, which is reflected in the magnitude term $E^{\frac{1}{2}}$ in (42). We also find that the process of Ekman pumping continues until the local velocity field $\delta\vec{v}$ becomes equal to the boundary velocity \vec{v}_B . This is followed by spin-up of the entire interior on much larger time scales of $O(E^{-1}\Omega^{-1})$. Furthermore, the magnitude term of $E^{\frac{1}{2}}$ can be understood in terms of scaling arguments. The viscous term in the dimensionless Navier-Stokes equation (7) is given as

$$FE\nabla^2 \sim FE \left[\frac{1}{\delta L} \right]^2 \sim O(F), \quad (43)$$

where δL is the scale of the thickness of the viscous boundary layer. Clearly, from the relation given above, $\delta L = O(E^{\frac{1}{2}})$; also see the detailed discussion by Abney and Epstein [17] on this subject. The characteristic thickness of the boundary layer and the time scale of Ekman pumping are both attributable to the magnitude term $E^{\frac{1}{2}}$ in (42).

G. The characteristic equation

Considering the $O(E^0)$ and $O(E^{\frac{1}{2}})$ solutions obtained in the previous sections, we combine them to write the following differential equation with terms up to orders $O(E^{\frac{1}{2}})$ and $O(F^0)$:

$$\begin{aligned} \frac{1}{r} \frac{\partial}{\partial r} \left[r \frac{\partial \chi}{\partial r} \right] + \frac{1}{r^2} \frac{\partial^2 \chi}{\partial \phi^2} - \left[\frac{4\eta(z)K_s(z)}{N^2(z)} \right] \frac{\partial \chi}{\partial z} + \frac{4\eta(z)}{N^2(z)} \frac{\partial^2 \chi}{\partial z^2} \\ = \left[\frac{\partial_z \eta - \partial_z^2 \eta}{N^2(z)} \right] \chi. \end{aligned} \quad (44)$$

The above characteristic equation can be solved via the standard *method of separation of variables* to yield

$$\begin{aligned} \chi(r, \phi, z, t) = \sum_{\alpha=0}^{\infty} \sum_{\gamma=1}^{\infty} J_\alpha(\lambda_{\alpha\gamma} r) \left[\frac{A_{\alpha\gamma}(t) - iB_{\alpha\gamma}(t)}{2} \right. \\ \left. \times e^{i\alpha\phi} + \frac{A_{\alpha\gamma}(t) + iB_{\alpha\gamma}(t)}{2} e^{-i\alpha\phi} \right] Z_{\alpha\gamma}(z), \end{aligned} \quad (45)$$

where $\lambda_{\alpha\gamma}$ is the γ th zero of the α th Bessel mode (J_α), and $A_{\alpha\gamma}(t)$, $B_{\alpha\gamma}(t)$ are the associated *Bessel-Fourier coefficients* which depend upon the assumed steady-state solution, which we will see shortly. The flow is constrained by a trivial boundary condition which requires no penetration through the sidewalls, i.e., $\delta v_r^{(0)}|_{r=1} = 0$. This simply translates to $\partial_\phi \chi|_{r=1} = 0$ for $\forall \phi$'s, via (31). Moreover, $Z_{\alpha\gamma}(z)$ is the solution to the following differential equation:

$$\begin{aligned} \frac{4\eta(z)}{N^2(z)} \frac{\partial^2 Z_{\alpha\gamma}(z)}{\partial z^2} - \frac{4\eta(z)K_s(z)}{N^2(z)} \frac{\partial Z_{\alpha\gamma}(z)}{\partial z} \\ - \left[\frac{\partial_z \eta - \partial_z^2 \eta}{N^2(z)} + \lambda_{\alpha\gamma}^2 \right] Z_{\alpha\gamma}(z) = 0, \end{aligned} \quad (46)$$

which depends on N^2 , which in turn depends exclusively on K_s and η . When K_s (or, v_{eq}) and η (or, v_c) are constants, $Z_{\alpha\gamma}(z)$ takes the simple form given below,

$$Z_{\alpha\gamma}(z) = \frac{(FN^2 - \mathcal{B}_-)e^{\mathcal{B}_+z} - (FN^2 - \mathcal{B}_+)e^{\mathcal{B}_-z}}{(FN^2 - \mathcal{B}_-)e^{\mathcal{B}_+z} - (FN^2 - \mathcal{B}_+)e^{\mathcal{B}_-z}}, \quad (47)$$

where

$$\mathcal{B}_\pm = \frac{1}{2} [K_s \pm (K_s^2 + \eta^{-1}N^2\lambda_{\alpha\gamma}^2)^{\frac{1}{2}}]. \quad (48)$$

It must be noted that, following [5], we have temporarily—and seemingly arbitrarily⁵—assumed $Z_{\alpha\gamma}(1) = 1$. Moreover, we also assume $v_z|_{z=0} \sim v_z^{(1)}|_{z=0} = 0$ to ensure symmetric flow across the $z = 0$ plane,⁶ given the relation prescribed. This is precisely the result obtained by van Eysden and Melatos [5] and Bennett *et al.* [15].

H. Temporal evolution

The temporal evolution of Ekman pumping is governed by the boundary condition given in (42) [5,17]. Taking the

⁵The function $Z_{\alpha\gamma}(z)$ must be explicitly renormalized to lie in the range $[0, 1]$, since (41) dictates that χ —as a dimensionless variable—must be, at most, of the order $O(E^0) \sim 1$. This requires $Z_{\alpha\gamma}(z)$ to be of the same order of magnitude.

⁶The boundary condition on axial flow, i.e., setting $v_z|_{z=0} \sim v_z^{(1)}|_{z=0} = 0$ in (39), is equivalent to specifying $Z_{\alpha\gamma}(z)$ at $z = 0$.

first-order derivative of (42) and using the results from the $O(E^0)$ and $O(E^{\frac{1}{2}})$ solutions, we find the exponentially decaying time dependence⁷ of χ ,

$$\chi(r, \phi, z, t) = \sum_{\alpha=0}^{\infty} \sum_{\gamma=1}^{\infty} J_{\alpha}(\lambda_{\alpha\gamma} r) \left[\frac{A_{\alpha\gamma} - iB_{\alpha\gamma}}{2} \times e^{i\alpha\phi} + \frac{A_{\alpha\gamma} + iB_{\alpha\gamma}}{2} e^{-i\alpha\phi} \right] Z_{\alpha\gamma}(z) e^{-\omega_{\alpha\gamma} t}, \quad (49)$$

where, momentarily assuming $Z_{\alpha\gamma}(1)$ to be an arbitrary value that we will define shortly, we get

$$\omega_{\alpha\gamma} = \frac{1}{4F} \lambda_{\alpha\gamma}^2 Z_{\alpha\gamma}(1) \left[\frac{\eta(1)}{FN^2(1)} \frac{\partial Z_{\alpha\gamma}}{\partial z} \Big|_{z=1} + \left\{ \frac{-\partial_z \eta|_{z=1}}{FN^2(1)} - 1 \right\} Z_{\alpha\gamma}(1) \right]^{-1}. \quad (50)$$

Note that, for the simple case where $K_s(z), \eta \sim \text{constant}$ and $Z_{\alpha\gamma}(1) = 1$, (50) reduces to

$$\omega_{\alpha\gamma} = \frac{\lambda_{\alpha\gamma}^2 [(FN^2 - \mathcal{B}_-) e^{\mathcal{B}_+} - (FN^2 - \mathcal{B}_+) e^{\mathcal{B}_-}]}{(4FK + \lambda_{\alpha\gamma}^2)(e^{\mathcal{B}_+} - e^{\mathcal{B}_-})}. \quad (51)$$

Furthermore, given the explicit dependence of χ on time, we integrate (49) over $t \in [t, \infty)$ and get

$$\begin{aligned} \frac{\delta p^{(0)}(r, \phi, z, t)}{\rho(z)} &= \frac{\delta p_{t \rightarrow \infty}^{(0)}(r, \phi, z)}{\rho(z)} + \sum_{\alpha=0}^{\infty} \sum_{\gamma=1}^{\infty} \omega_{\alpha\gamma}^{-1} \\ &\times J_{\alpha}(\lambda_{\alpha\gamma} r) [A_{\alpha\gamma} \cos(\alpha\phi) + B_{\alpha\gamma} \sin(\alpha\phi)] \\ &\times Z_{\alpha\gamma}(z) e^{-\omega_{\alpha\gamma} t}, \end{aligned} \quad (52)$$

where the first term on the right-hand side is the constant of integration evaluated at $t \rightarrow \infty$, i.e., the steady-state pressure profile of the spun-up cylinder. The relation given in (52) encodes the variation of pressure perturbations up to the leading order in magnitude as a function of time.

I. Initial and final conditions

We are left with one intrinsic degree of freedom in our model in the form of initial and final conditions in time, i.e., the state of perturbations immediately following the glitch at $t = 0$ and when Ekman pumping stops as $t \rightarrow \infty$, respectively. In principle, we only require one boundary condition in time—once $A_{\alpha\gamma}, B_{\alpha\gamma}$ are known—since the state of modes at $t \rightarrow \infty$ is coupled to their state at $t = 0$ by the relation (52), and vice versa. In this case, however, we require both the initial and final conditions in time to calculate $A_{\alpha\gamma}, B_{\alpha\gamma}$ since they are unknown. For example, two of the most general choices are (a) one can assume a

scenario where the perturbation modes continuously grow from an axisymmetric state in the post-glitch phase at $t = 0$ and reach a steady nonaxisymmetric state as $t \rightarrow \infty$ and remain in that state. This leads to emission of gravitational waves even in the steady state at $t \rightarrow \infty$ and is somewhat unphysical. In fact, this equates to the scenario of “semi-rigidity,” where the top and bottom faces of the cylinder rotate differentially at $t \rightarrow \infty$, potentially causing the crust to crack [5]. On the contrary, (b) an alternative scenario is when the perturbation modes are instantaneously excited at $t = 0$ and eventually decay as $t \rightarrow \infty$, which is more physical than the former choice. This choice disallows any residual nonaxisymmetry in the bulk, ensures zero residual steady-state emission, and also incorporates the feature of rigidity between the two faces of the cylinder [15]. Both of these possibilities are encoded in our choice of assumed boundary conditions at $t = 0$ and $t \rightarrow \infty$. Hence, we assume the more physical set of initial and final conditions where the modes originate arbitrarily and instantaneously at $t = 0$, and decay from some unknown initial value δP_0 to a symmetric steady-state δP_{∞} as $t \rightarrow \infty$ according to (52). Note that the steady-state solution at $t \rightarrow \infty$ is an axisymmetric state with no angular or z dependence but only radial dependence, given as $\delta P_{\infty} = r^2$ in dimensionless form [15]. This axisymmetric state does not lead to any gravitational wave emission, as previously stated.

Finally, in order to calculate $A_{\alpha\gamma}, B_{\alpha\gamma}$, we write

$$\begin{aligned} \delta P_0 &= \delta P_{\infty} + \sum_{\alpha=0}^{\infty} \sum_{\gamma=1}^{\infty} \omega_{\alpha\gamma}^{-1} J_{\alpha}(\lambda_{\alpha\gamma} r) \\ &\times [A_{\alpha\gamma} \cos(\alpha\phi) + B_{\alpha\gamma} \sin(\alpha\phi)] Z_{\alpha\gamma}(z) \\ &= \sum_{\alpha=0}^{\infty} C_{\alpha} r^{\alpha} (r^2 - 1) \cos(\alpha\phi) Z_{\alpha\gamma}(z), \end{aligned} \quad (53)$$

where, whenever suitable from this point onward, we will abbreviate, for simplicity,

$$\delta P_{t'} \equiv \frac{\delta p_{t \rightarrow t'}^{(0)}(r, \phi, z)}{\rho(z)}.$$

The assumed form of the initial arbitrary perturbations δP_0 in (53) is a sum of nonaxisymmetric modes satisfying the boundary conditions [15]. C_{α} represents the relative weights of modes with respect to the loudest mode, excited at $t = 0$, and it will be set equal to 1 in the calculations in Sec. IV. Note that any assumed form of δP_0 must be constrained by the boundary conditions in space; i.e., no penetration is allowed across the sidewalls, and the assumed form must be a solution to the Navier-Stokes equation by satisfying the relations in (17)–(19). Our assumption of δP_0 guarantees the decay of all modes at $t \rightarrow \infty$, while it also ensures that the flow vanishes at the lateral surface at $r = L$. We have assumed trivial z

⁷Refer to Sec. A of the Appendix for details.

dependence and ϕ dependence in (53) for simplicity [5,15], without potentially corrupting the generality of the solutions. The associated Bessel-Fourier coefficients $A_{\alpha\gamma}$ and $B_{\alpha\gamma}$ can now be calculated⁸ as an implicit function of z as follows:

$$\begin{aligned} A_{\alpha\gamma} &= \frac{2\omega_{\alpha\gamma}}{\pi J_{\alpha+1}^2(\lambda_{\alpha\gamma})} \int_0^{2\pi} d\phi \int_0^1 dz \int_0^1 r dr \\ &\quad \times J_\alpha(\lambda_{\alpha\gamma} r) \cos(\alpha\phi) [\delta P_0 - \delta P_\infty] Z_{\alpha\gamma}^{-1}(z) \\ &= \frac{2C_\alpha \omega_{\alpha\gamma}}{J_{\alpha+1}^2(\lambda_{\alpha\gamma})} \int_0^1 dr r^{\alpha+1} (r^2 - 1) J_\alpha(\lambda_{\alpha\gamma} r), \end{aligned} \quad (54)$$

and

$$\begin{aligned} B_{\alpha\gamma} &= \frac{2\omega_{\alpha\gamma}}{\pi J_{\alpha+1}^2(\lambda_{\alpha\gamma})} \int_0^{2\pi} d\phi \int_0^1 dz \int_0^1 r dr \\ &\quad \times J_\alpha(\lambda_{\alpha\gamma} r) \sin(\alpha\phi) [\delta P_0 - \delta P_\infty] Z_{\alpha\gamma}^{-1}(z) = 0. \end{aligned} \quad (55)$$

In principle, the Bessel-Fourier coefficients may not be constants. In fact, they could be functions of ϕ and z , depending on the chosen initial conditions in (53). However, since we chose trivial dependence on ϕ and z in our assumed initial conditions in (53), $A_{\alpha\gamma}$ and $B_{\alpha\gamma}$ remain constant. The first few values of $A_{\alpha\gamma}$ are $A_{11} = -0.706\omega_{11}$, $A_{21} = -0.521\omega_{21}$, $A_{12} = 0.154\omega_{12}$, and $A_{22} = 0.148\omega_{22}$.

J. Final solutions

We restore the dimensions and calculate the final *velocity*, *density*, and *pressure* fields in the inertial rest frame instead of the rotating frame. The density profile in the inertial frame is given as

$$\begin{aligned} \rho(r, \phi, z, t) &= \rho_0 \rho_e(z/L) + \rho_0 \frac{(\delta\Omega)\Omega L}{g} \\ &\quad \times \sum_{\alpha=0}^{\infty} \sum_{\gamma=1}^{\infty} \omega_{\alpha\gamma}^{-1} C_\alpha A_{\alpha\gamma} J_\alpha\left(\frac{\lambda_{\alpha\gamma} r}{L}\right) \cos[\alpha(\phi - \Omega t)] \\ &\quad \times \partial_z [-L Z_{\alpha\gamma}(z/L) \rho_e(z/L)] e^{-E^{\frac{1}{2}} \omega_{\alpha\gamma} \Omega t}, \end{aligned} \quad (56)$$

whereas, from (34),

$$\begin{aligned} \delta\rho_{t \rightarrow 0}^{(0)}(r, \phi, z) &= -\partial_z [\rho(z) \delta P_0] \\ &= -\left[\sum_{\alpha=0}^{\infty} C_\alpha r^\alpha (r^2 - 1) \cos(\alpha\phi) \right] \frac{\partial[\rho(z)]}{\partial z}. \end{aligned} \quad (57)$$

$\delta v_r^{(0)}(r, \phi, z, t \rightarrow 0)$ and $\delta v_\phi^{(0)}(r, \phi, z, t \rightarrow 0)$ can be similarly calculated from (31) and (32), respectively. The pressure profile and the velocity field up to order $O(E^{\frac{1}{2}})$ are given as

$$p(r, \phi, z, t) = \rho_0 g L p_e(z/L) + \left[\rho_0 (\delta\Omega) \Omega L^2 \sum_{\alpha=0}^{\infty} \sum_{\gamma=1}^{\infty} \omega_{\alpha\gamma}^{-1} C_\alpha A_{\alpha\gamma} J_\alpha\left(\frac{\lambda_{\alpha\gamma} r}{L}\right) Z_{\alpha\gamma}(z/L) \times \cos[\alpha(\phi - \Omega t)] \rho_e(z/L) e^{-E^{\frac{1}{2}} \omega_{\alpha\gamma} \Omega t} \right], \quad (58)$$

$$\delta v_r \sim \delta v_r^{(0)}(r, \phi, z, t) = \frac{1}{2} (\delta\Omega) L^2 \sum_{\alpha=0}^{\infty} \sum_{\gamma=1}^{\infty} \frac{\alpha}{r} \omega_{\alpha\gamma}^{-1} C_\alpha \times A_{\alpha\gamma} J_\alpha\left(\frac{\lambda_{\alpha\gamma} r}{L}\right) \cos[\alpha(\phi - \Omega t)] Z_{\alpha\gamma}(z/L) e^{-E^{\frac{1}{2}} \omega_{\alpha\gamma} \Omega t}, \quad (59)$$

$$\delta v_\phi \sim \delta v_\phi^{(0)}(r, \phi, z, t) = \Omega r + \frac{1}{2} (\delta\Omega) L \sum_{\alpha=0}^{\infty} \sum_{\gamma=1}^{\infty} \omega_{\alpha\gamma}^{-1} \times C_\alpha A_{\alpha\gamma} \lambda_{\alpha\gamma} \partial_r \left[L J_\alpha\left(\frac{\lambda_{\alpha\gamma} r}{L}\right) \right] \cos[\alpha(\phi - \Omega t)] \times Z_{\alpha\gamma}(z/L) e^{-E^{\frac{1}{2}} \omega_{\alpha\gamma} \Omega t}, \quad (60)$$

and⁹

$$\begin{aligned} \delta v_z \sim v_z^{(1)}(r, \phi, z, t) &= \frac{1}{\text{FN}^2(z)} \frac{\partial \chi}{\partial z} - \chi \\ &= O(E^{\frac{1}{2}}) \quad (\text{in dimensionless units}). \end{aligned} \quad (61)$$

⁸Refer to Sec. B in the Appendix for details.

⁹We have left the expression in condensed form since the contribution is of the order $O(E^{\frac{1}{2}})$ only, which is lower than the magnitudes we want to explore.

IV. GRAVITATIONAL WAVE EMISSION

In this section, we describe the gravitational wave emission from mass-quadrupole and current-quadrupole moments of the nonaxisymmetric flow derived in Sec. III.

A. Gravitational wave emission via mass quadrupole

The density, pressure, and velocity fields calculated in the previous section lead to gravitational wave emission if the mass distribution and fluid flow are nonaxisymmetric in

nature. Gravitational wave emission is attributable to a nonaxisymmetric distribution of mass that has a nonzero mass-quadrupole moment with an at least second-order nonvanishing time derivative. We derive the gravitational wave emission for the leading-order quadrupole term ($\alpha = 2$) straightaway¹⁰ for the $+$ and \times polarizations for a *polar observer*—for an observer located at a distance d_s along the axis of rotation of the neutron star,

$$h_+^{\text{MP}}(t) = h_0^{\text{M}} \sum_{\gamma=1}^{\infty} \kappa_{2\gamma} [-4\omega_{2\gamma} E_{2\gamma}^{\frac{1}{2}} \sin(2\Omega t) + (4 - E\omega_{2\gamma}^2) \cos(2\Omega t)] e^{-E_{2\gamma}^{\frac{1}{2}} \omega_{2\gamma} \Omega t}, \quad (62)$$

$$h_{\times}^{\text{MP}}(t) = h_0^{\text{M}} \sum_{\gamma=1}^{\infty} \kappa_{2\gamma} [-4\omega_{2\gamma} E_{2\gamma}^{\frac{1}{2}} \cos(2\Omega t) - (4 - E\omega_{2\gamma}^2) \sin(2\Omega t)] e^{-E_{2\gamma}^{\frac{1}{2}} \omega_{2\gamma} \Omega t}, \quad (63)$$

where the full expression of $\kappa_{\alpha\gamma}$ is too lengthy to quote here and is given in Sec. E of the Appendix and C_α is set to 1. The characteristic dimensionless strain h_0 and $t_{\alpha\gamma}$ —the relaxation time scale for the $\{\alpha, \gamma\}$ th mode—are given as

$$h_0^{\text{M}} = \pi \rho_0 \Omega^4 L^6 \epsilon \frac{G}{c^4 d_s g}, \quad (64)$$

$$t_{\alpha\gamma} = E^{-\frac{1}{2}} \Omega^{-1} \omega_{\alpha\gamma}^{-1}, \quad (65)$$

where $\kappa_{2\gamma}$ and h_0^{M} are both constant quantities. We transform the expressions (62) and (63) for time-series amplitudes to the more useful Fourier space for a polar observer as follows¹¹:

$$|h_+^{\text{MP}}(\omega)|^2 = h_0^{\text{M}2} \sum_{\gamma=1}^{\infty} |\kappa_{2\gamma}|^2 \{ [t_{2\gamma}^{-2} (4 + t_{2\gamma}^{-2} \Omega^{-2})^2 + \omega^2 (4 - t_{2\gamma}^{-2} \Omega^{-2})^2] [(4\Omega^2 + t_{2\gamma}^{-2} - \omega^2)^2 + (2\omega t_{2\gamma}^{-1})^2]^{-1} \}, \quad (66)$$

$$|h_{\times}^{\text{MP}}(\omega)|^2 = h_0^{\text{M}2} \sum_{\gamma=1}^{\infty} |\kappa_{2\gamma}|^2 \{ [4\Omega^2 (4 + t_{2\gamma}^{-2} \Omega^{-2})^2 + 16\omega^2 t_{2\gamma}^{-2} \Omega^{-2}] [(4\Omega^2 + t_{2\gamma}^{-2} - \omega^2)^2 + (2\omega t_{2\gamma}^{-1})^2]^{-1} \}. \quad (67)$$

Clearly, $|h_+^{\text{MP}}(\omega)|$ and $|h_{\times}^{\text{MP}}(\omega)|$ exhibit resonance at $\omega_{\text{R}}^2 = 4\Omega^2 + t_{2\gamma}^{-2}$. A similar calculation can be made for an *equatorial observer*, and the corresponding results are given as

$$h_+^{\text{ME}}(t) = \frac{1}{2} h_0^{\text{M}} \sum_{\gamma=1}^{\infty} \kappa_{2\gamma} [-4\omega_{2\gamma} E_{2\gamma}^{\frac{1}{2}} \sin(2\Omega t) + (4 - E\omega_{2\gamma}^2) \cos(2\Omega t)] e^{-E_{2\gamma}^{\frac{1}{2}} \omega_{2\gamma} \Omega t}, \quad (68)$$

$$h_{\times}^{\text{ME}}(t) = 2h_0^{\text{M}} \sum_{\gamma=1}^{\infty} \kappa_{1\gamma} [2\omega_{1\gamma} E_{1\gamma}^{\frac{1}{2}} \cos(\Omega t) + (1 - E\omega_{1\gamma}^2) \sin(\Omega t)] e^{-E_{1\gamma}^{\frac{1}{2}} \omega_{1\gamma} \Omega t}. \quad (69)$$

It is important to note the change of oscillating frequency for the \times polarization from 2Ω in the case of a polar observer to Ω in the case of an equatorial observer. Furthermore, additional 1γ modes are seen by an equatorial observer and appear besides the 2γ modes that appear in the emission spectrum. In Fourier space for an equatorial observer, we have

$$|h_+^{\text{ME}}(\omega)|^2 = \frac{1}{4} h_0^{\text{M}2} \sum_{\gamma=1}^{\infty} |\kappa_{2\gamma}|^2 \{ [t_{2\gamma}^{-2} (4 + t_{2\gamma}^{-2} \Omega^{-2})^2 + \omega^2 (4 - t_{2\gamma}^{-2} \Omega^{-2})^2] [(4\Omega^2 + t_{2\gamma}^{-2} - \omega^2)^2 + (2\omega t_{2\gamma}^{-1})^2]^{-1} \}, \quad (70)$$

$$|h_{\times}^{\text{ME}}(\omega)|^2 = 4h_0^{\text{M}2} \sum_{\gamma=1}^{\infty} |\kappa_{1\gamma}|^2 \{ [\Omega^2 (1 + t_{1\gamma}^{-2} \Omega^{-2})^2 + 4\omega^2 t_{1\gamma}^{-2} \Omega^{-2}] [(\Omega^2 + t_{1\gamma}^{-2} - \omega^2)^2 + (2\omega t_{1\gamma}^{-1})^2]^{-1} \}. \quad (71)$$

In this case, $|h_+^{\text{ME}}(\omega)|$ exhibits resonance at $\omega_{\text{R}}^2 = 4\Omega^2 + t_{2\gamma}^{-2}$, while $|h_{\times}^{\text{ME}}(\omega)|$ exhibits resonance at $\omega_{\text{R}}^2 = \Omega^2 + t_{1\gamma}^{-2}$. It is worth noting that the factors $\kappa_{1\gamma}$, $\kappa_{2\gamma}$ decrease in magnitude with an increasing index γ , and we can truncate the above expressions at leading order, $\gamma = 1$. The maximum order-of-magnitude value of the amplitude of the emitted gravitational waves for both polarizations at a given frequency ω then depends strongly on the characteristic magnitude h_0^{M} and its amplification by the frequency terms in the Fourier transforms. There also exists a weak dependency on the prefactors $|\kappa_{1\gamma}|$ and $|\kappa_{2\gamma}|$.¹² In Figs. 2 and 3 above, we

¹⁰Refer to Sec. C in the Appendix for details of the calculation.

¹¹ δ_{D} is the Kronecker delta function with units of Hz^{-1} .

¹²The “weak” dependency in this case refers to the fact that $|\kappa_{1\gamma}|$ and $|\kappa_{2\gamma}|$ are not as sensitive to variations in K_s or N^2 , as we will see in later sections.

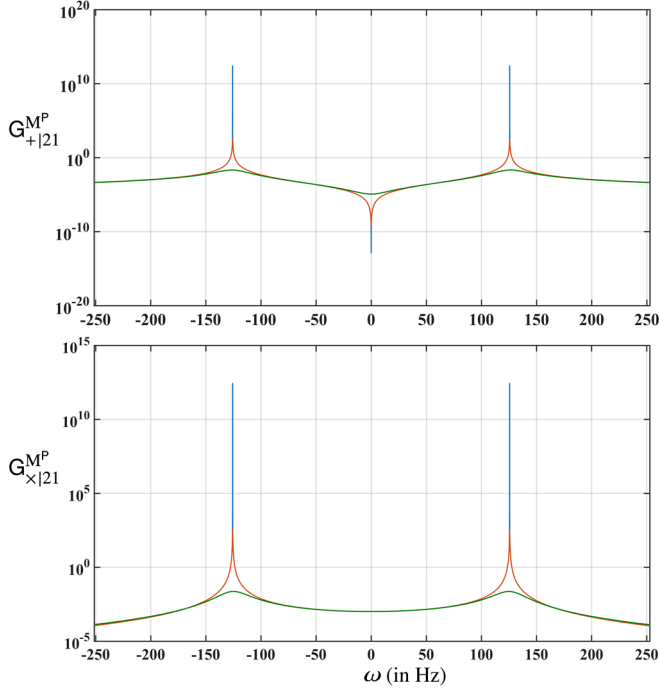


FIG. 2. Frequency characteristics of emitted signals for a polar observer: three different sets of data are plotted for the rotational frequency Ω of 10 Hz and $\partial_z \eta \sim 10^{-11}$. The respective color-coded time scales are 9.8, 1.1×10^{-4} , and 8.5×10^{-7} days. The corresponding resonant frequencies are ± 125.66371 , ± 125.66375 , and ± 126.39611 Hz. Note that values of the time scales are calculated for specifically chosen physical parameters of the system— v_c , $\partial_z \eta$, v_{eq} , K , and F —in order to cover a large range of time scales. A similar result for an equatorial observer is shown in Fig. 3.

plot the frequency characteristics¹³ of the emitted signal amplitudes for $|h_+^{MP}(\omega)|$, $|h_x^{MP}(\omega)|$, $|h_+^{ME}(\omega)|$, and $|h_x^{ME}(\omega)|$.

B. Gravitational wave emission via current quadrupole

Gravitational wave emission, as traditionally understood, from the mass quadrupole occurs when the associated oscillating mass-quadrupole moment excites gravitational waves. However, time variation in the intrinsic mass distribution (also known as the *mass currents*) of the bulk matter could also lead to gravitational wave radiation through “current-quadrupole” contribution [15,27]. This effect is a subset of the *gravitomagnetic effects*—the electromagnetic equivalent in gravitation. Similar to the case of electromagnetism, where electric charges and current multipoles emit electromagnetic radiation, time-varying mass-current multipoles also emit gravitational wave radiation, in addition to the well-known emission

¹³In order to show the frequency characteristics, we abbreviate the remaining factors for simplicity, such that $\left[\frac{h_{\pm}^Y(\omega)}{h_0^L |\kappa_{\alpha\gamma}|}\right]^2 \equiv G_{\mp|\alpha\gamma}^{LY}$.

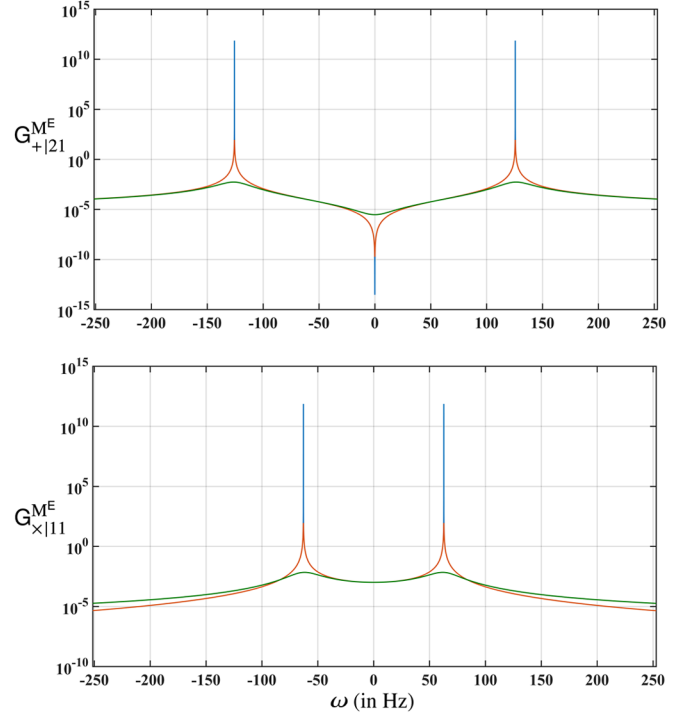


FIG. 3. Frequency characteristics of emitted signals for an equatorial observer: three different sets of data are plotted for the rotational frequency Ω of 10 Hz and $\partial_z \eta \sim 10^{-11}$. The respective color-coded time scales are 9.8, 1.1×10^{-4} , and 8.5×10^{-7} days. Moreover, the corresponding resonant frequencies for \times polarization are ± 62.83186 , ± 62.83188 , ± 63.19805 Hz, whereas the resonant frequencies for the $+$ polarization remain exactly the same as they were for the case of a polar observer. The other physical parameters are chosen to be the same as in Fig. 2.

from mass-quadrupole moment. Straightaway, we produce the expressions for the $+$ and \times polarization following Thorne [27], Melatos and Peralta [28], and Bennett *et al.* [15] for a polar observer as follows¹⁴:

$$\begin{aligned} h_+^{CP}(t) &= h_0^C \sum_{\gamma=1}^{\infty} V_{2\gamma} [-4t_{2\gamma}^{-1} \Omega^{-1} \cos(2\Omega t) \\ &\quad - (4 - t_{2\gamma}^{-2} \Omega^{-2}) \sin(2\Omega t)] e^{-t_{2\gamma}^{-1} t}, \\ h_x^{CP}(t) &= h_0^C \sum_{\gamma=1}^{\infty} V_{2\gamma} [-4t_{2\gamma}^{-1} \Omega^{-1} \sin(2\Omega t) \\ &\quad + (4 - t_{2\gamma}^{-2} \Omega^{-2}) \cos(2\Omega t)] e^{-t_{2\gamma}^{-1} t}, \end{aligned} \quad (72)$$

and, for an equatorial observer, by

¹⁴Refer to Sec. D in the Appendix for further details of the calculation, and for expressions of the prefactors $V_{1\gamma}$ and $V_{2\gamma}$.

$$\begin{aligned}
h_+^{\text{CE}}(t) &= 2h_0^{\text{C}} \sum_{\gamma=1}^{\infty} V_{1\gamma} [2t_{1\gamma}^{-1} \Omega^{-1} \cos(\Omega t) \\
&\quad + (1 - t_{1\gamma}^{-2} \Omega^{-2}) \sin(\Omega t)] e^{-t_{1\gamma}^{-1} t}, \\
h_{\times}^{\text{CE}}(t) &= \frac{1}{2} h_0^{\text{C}} \sum_{\gamma=1}^{\infty} V_{2\gamma} [-4t_{2\gamma}^{-1} \Omega^{-1} \sin(2\Omega t) \\
&\quad + (4 - t_{2\gamma}^{-2} \Omega^{-2}) \cos(2\Omega t)] e^{-t_{2\gamma}^{-1} t}, \quad (73)
\end{aligned}$$

where

$$h_0^{\text{C}} = 2\pi\rho_0\Omega^3 L^6 \epsilon \frac{G}{3c^5 d_s}. \quad (74)$$

Note that we have restricted ourselves to the leading-order quadrupole term $l = 2$ of the mass-current multipole expansion. Once more, we write the above expressions for polar and equatorial observers in the Fourier space. In the case of a polar observer, this reduces to

$$\begin{aligned}
|h_+^{\text{CP}}(\omega)|^2 &= h_0^{\text{C}2} \sum_{\gamma=1}^{\infty} |V_{2\gamma}|^2 \{ [4\Omega^2(4 + t_{2\gamma}^{-2} \Omega^{-2})^2 \\
&\quad + 16\omega^2 t_{2\gamma}^{-2} \Omega^{-2}] [(4\Omega^2 + t_{2\gamma}^{-2} - \omega^2)^2 \\
&\quad + (2\omega t_{2\gamma}^{-1})^2]^{-1} \}, \quad (75)
\end{aligned}$$

$$\begin{aligned}
|h_{\times}^{\text{CP}}(\omega)|^2 &= h_0^{\text{C}2} \sum_{\gamma=1}^{\infty} |V_{2\gamma}|^2 \{ [t_{2\gamma}^{-2}(4 + t_{2\gamma}^{-2} \Omega^{-2})^2 \\
&\quad + \omega^2(4 - t_{2\gamma}^{-2} \Omega^{-2})^2] [(4\Omega^2 + t_{2\gamma}^{-2} - \omega^2)^2 \\
&\quad + (2\omega t_{2\gamma}^{-1})^2]^{-1} \}. \quad (76)
\end{aligned}$$

It should be noted that the resonant frequencies for the current-quadrupole contribution from $|h_+^{\text{MP}}(\omega)|$ and $|h_{\times}^{\text{MP}}(\omega)|$ are the same as they were for the mass-quadrupole contribution. Furthermore, for the case of equatorial observers,

$$\begin{aligned}
|h_+^{\text{CE}}(\omega)|^2 &= 4h_0^{\text{C}2} \sum_{\gamma=1}^{\infty} |V_{1\gamma}|^2 \{ [\Omega^2(1 + t_{1\gamma}^{-2} \Omega^{-2})^2 \\
&\quad + 4\omega^2 t_{1\gamma}^{-2} \Omega^{-2}] [(\Omega^2 + t_{1\gamma}^{-2} - \omega^2)^2 \\
&\quad + (2\omega t_{1\gamma}^{-1})^2]^{-1} \}, \quad (77)
\end{aligned}$$

$$\begin{aligned}
|h_{\times}^{\text{CE}}(\omega)|^2 &= \frac{1}{4} h_0^{\text{C}2} \sum_{\gamma=1}^{\infty} |V_{2\gamma}|^2 \{ [t_{2\gamma}^{-2}(4 + t_{2\gamma}^{-2} \Omega^{-2})^2 \\
&\quad + \omega^2(4 - t_{2\gamma}^{-2} \Omega^{-2})^2] [(4\Omega^2 + t_{2\gamma}^{-2} - \omega^2)^2 \\
&\quad + (2\omega t_{2\gamma}^{-1})^2]^{-1} \}. \quad (78)
\end{aligned}$$

We see that the emitted signals from the mass quadrupole and the current quadrupole are similar in nature in terms of

the resonant frequencies and the general behavior of the frequency responses.¹⁵ However, there is a notable switch in the + and \times polarizations. Additionally, $V_{1\gamma}$ and $V_{2\gamma}$ prefactors now appear instead of $\kappa_{1\gamma}$ and $\kappa_{2\gamma}$ ones, in addition to the different characteristic amplitudes. Last, the frequency characteristics for $|h_+^{\text{CP}}(\omega)|$, $|h_{\times}^{\text{CP}}(\omega)|$, $|h_{\times}^{\text{CE}}(\omega)|$, and $|h_+^{\text{CE}}(\omega)|$ follow the same shapes as shown previously in Figs. 2 and 3.

C. A verdict on parameter space

It is clear from the general expressions of $\kappa_{\alpha\gamma}$ (in Sec. E of the Appendix) and $V_{\alpha\gamma}$ (in Sec. D of the Appendix) that their calculations are cumbersome to perform unless we are able to make some simplifying assumptions. Ideally, one would like to explore the range of parameter space where the first derivative of η —i.e., $\partial_z \eta$ in (51)—and $\partial_z K_s$ are constants and follow

$$\begin{aligned}
|\partial_z \eta| \ll \text{FN}^2 \ll \eta < 1 \quad \text{for } \forall z \in (0, 1], |\partial_z K_s| \ll |K_s| \\
\text{for } \forall z \in (0, 1]. \quad (79)
\end{aligned}$$

Such a choice of a regime is physically reasonable and it makes the calculations analytically feasible, without compromising the generality of the model. These assumptions allow us to reduce the parameter space and explore the model in its simplest form. Meanwhile, since we do not have any prior functional forms of v_c and v_{eq} with respect to the z coordinate, we assume a simple scenario where v_c is linear in z and takes the form¹⁶

$$v_c(z) \sim v_c^0 + z \times \partial_z v_c, \quad (80)$$

while, at the same time, N^2 is taken to be a constant. These assumptions leave v_{eq} implicitly varying in z according to (28). It must be noted that this does not imply constancy of η . In fact, it is simply that $\partial_z \eta \sim 2v_c(z) \partial_z v_c$, and $\partial_z^2 \eta \sim 2(\partial_z v_c)^2$. Last, we are left with N^2 , v_c^0 , and $\partial_z v_c$ as free parameters in our model. K_s (or v_{eq}) in this case becomes a dependent parameter varying in z according to (28), as previously stated. Thus, we restrict ourselves to the domain where

¹⁵The characteristic amplitudes for the mass and current quadrupoles are related by $\frac{|h_0^{\text{C}}|}{|h_0^{\text{M}}|} = \frac{2g}{3\Omega c}$.

¹⁶Note that any functional form of $v_c(z)$ can be reduced to this expression at leading order as long as $|\partial_z v_c| \ll v_c^0$. This is equivalent to a “stiff” polytropic equation of state with the polytropic exponent $\gamma \rightarrow 1$.

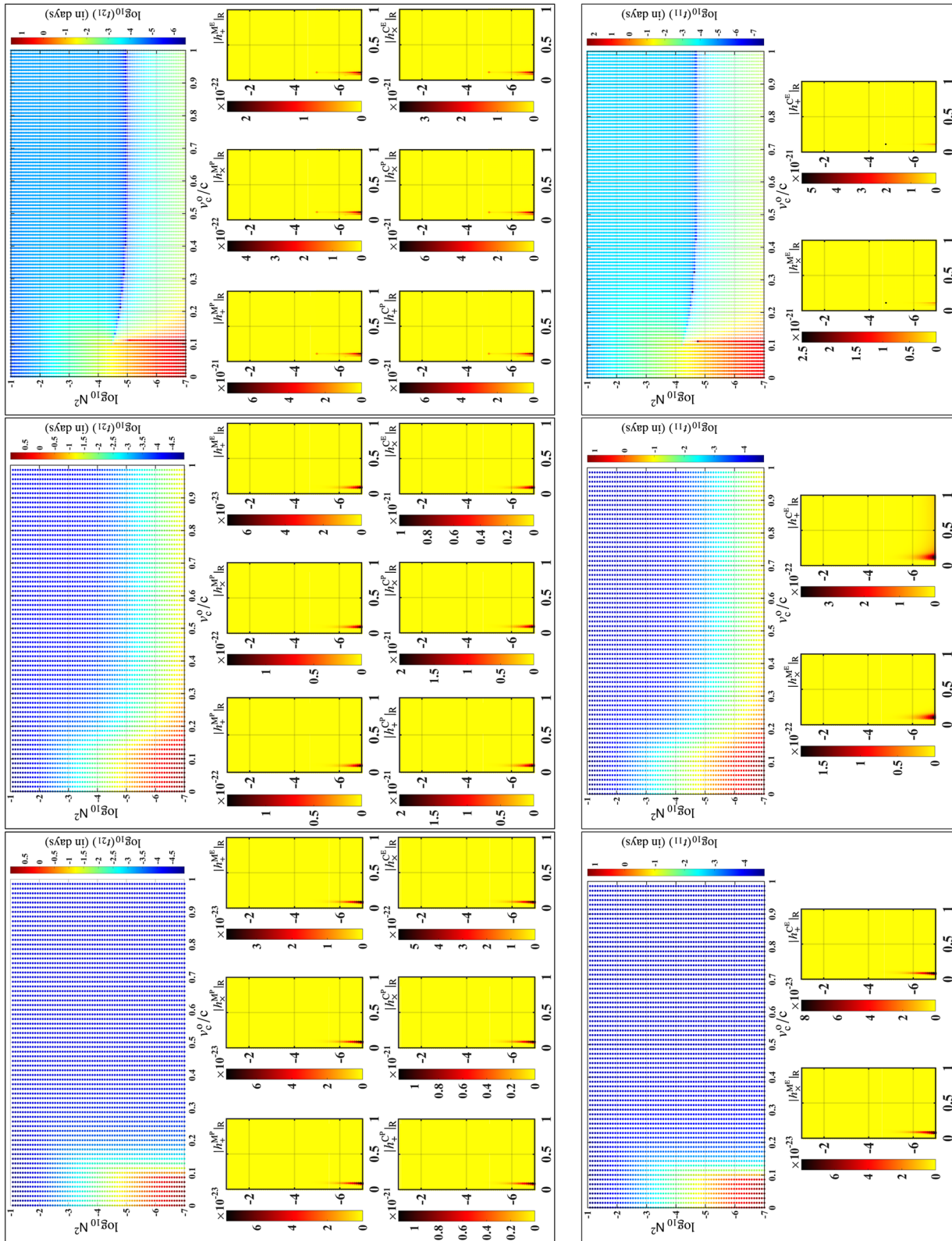


FIG. 4. Emitted gravitational wave strain (*turn page sideways*). (Top panel) Time scales for the t_{21} mode and the corresponding gravitational wave strain amplitudes for three sets of values for $\partial_z v_c$: 0 , $10^{-3}cL^{-1}$, $10^{-4}cL^{-1}$ (left to right), respectively. (Bottom panel) The t_{11} modes and corresponding gravitational wave strain amplitudes. The parameters are set to $f = 100$ Hz, $E = 10^{-7}$, $\epsilon = 10^{-4}$, $d_s = 1.0$ kpc, $L = 10^4$ m, $g = 10^{12}$ m/sec², $\rho_o = 10^{17}$ kg/m³. All positive time scales, as well as the corresponding emitted amplitudes, are marked with a \bullet , while the negative time scales and corresponding amplitudes are marked with a $+$. Negative time scales correspond to the scenario of growing modes²⁰.

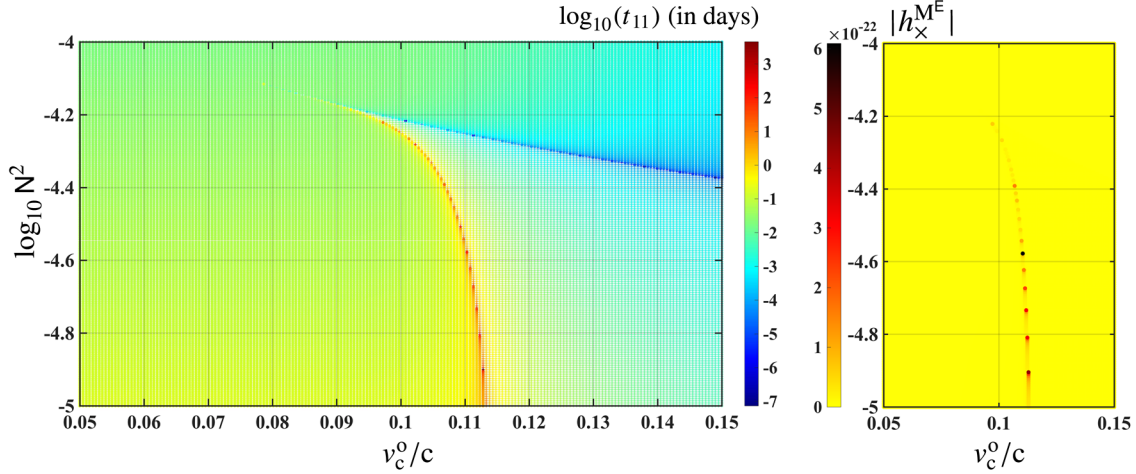


FIG. 5. Outlier enlarged. The characteristics of the parameter space in the vicinity of the apparent outlier in Fig. 4 for the case of $\partial_z v_c = -10^{-4} cL^{-1}$ (the rightmost panels in Fig. 4) are shown in higher resolution. All positive time scales as well as the corresponding emitted amplitudes are marked with a \bullet , while the negative time scales and the corresponding strain amplitudes are marked with a $+$.

$$\begin{aligned} |\partial_z v_c| \ll v_c^0 < 1 &\Rightarrow |\partial_z K_s| \ll |K_s|, \\ \partial_z \eta &\sim 2v_c^0 \partial_z v_c. \end{aligned} \quad (81)$$

Under such assumptions, the calculations for the factors $\kappa_{\alpha\gamma}$ and $V_{\alpha\gamma}$ become analytic and relatively simple.¹⁷ The simplification occurs because $\partial_z \eta$ is now invariant in z according to (81). To further validate our choice, we find that numerical errors dominate significantly when calculating $\kappa_{\alpha\gamma}$ and $V_{\alpha\gamma}$ numerically, especially toward the lower ranges of v_c^0 . These numerical errors are catalyzed by large corresponding magnitudes of K_s when v_c^0 becomes very small. This effect is shown in detail in Sec. F of the Appendix, where we have compared numerical and analytic results for $\kappa_{\alpha\gamma}$ and $V_{\alpha\gamma}$ while assuming (81) to be true. In a nutshell, the analytic approximation (81) enables us to selectively explore the more crucial aspects of the improved model, such as $\partial_z v_c$, while ignoring the less crucial degrees of freedom of the system, such as the spatial variations in N^2 . The complete reduced expressions for $\kappa_{\alpha\gamma}$ and $V_{\alpha\gamma}$ are given in Sec. E of the Appendix.

It must be noted that such an assumption of constancy of $\partial_z \eta$ is not applied while calculating $\omega_{\alpha\gamma}$ or the corresponding time scales $t_{\alpha\gamma}$ via (50). However, the time scales $t_{\alpha\gamma}$ are not prone to errors from numerical computations, as opposed to $\kappa_{\alpha\gamma}$ and $V_{\alpha\gamma}$. It remains straightforward to compute them numerically and accurately. Nonetheless, the approximated analytic expression for the time scales is given in Sec. E of the Appendix [see (A38)].

V. TIME SCALES OF EMITTED SIGNALS AND CORRESPONDING AMPLITUDES

In this section, we explore the decay time scales of the emitted signals. We see from the expressions in (62)–(69) for the mass-quadrupole contribution, and (72)–(75) for the current-quadrupole contribution, that the decay time scale $t_{\alpha\gamma}$ for a given $\{\alpha, \gamma\}$ mode—as defined previously in (64)—is given as

$$t_{\alpha\gamma} = E^{-\frac{1}{2}} \Omega^{-1} \omega_{\alpha\gamma}^{-1}. \quad (82)$$

The emitted gravitational wave signal amplitude at a given frequency ω depends intrinsically on the time scale; this is shown in the expressions (62)–(78). Following the discussion of the previous section, we have three independent parameters to vary: v_c^0 , $\partial_z v_c$, and N^2 , under the analytic approximations introduced by (81). In Fig. 4, we plot the characteristics for the involved time scales t_{11} and t_{21} , and the corresponding gravitational wave amplitudes for mass-quadrupole and current-quadrupole contributions at resonant frequencies, i.e., $\omega = \omega_R$ (denoted by the subscript \mathbf{R}). Note that the resonant frequencies ω_R are also a function of $t_{\alpha\gamma}$, as shown in Sec. IV A. This corresponds to the effect where $|h_x^{ME}|$, $|h_+^{CE}|$ emit at different resonant frequencies and different time scales than $|h_x^{MP}|$, $|h_+^{MP}|$, $|h_+^{ME}|$, $|h_x^{CP}|$, $|h_+^{CP}|$, and $|h_x^{CE}|$, as shown in Fig. 4. We also find that only a very small fraction of mechanical energy [$O(10^{-9} - 10^{-7})$] from the glitch is converted into gravitational wave emission.¹⁸

Note that, in the case of $\partial_z v_c < 0$ in Fig. 4 (the rightmost panels), the apparent outlier in the plots for $\partial_z v_c = -10^{-4} cL^{-1}$ is an artifact of low resolution in parameter

¹⁷See Sec. E of the Appendix for details, and for full expressions of $\kappa_{\alpha\gamma}$ and $V_{\alpha\gamma}$.

¹⁸The energetics of the emitted amplitudes is discussed in detail in Sec. VI B.

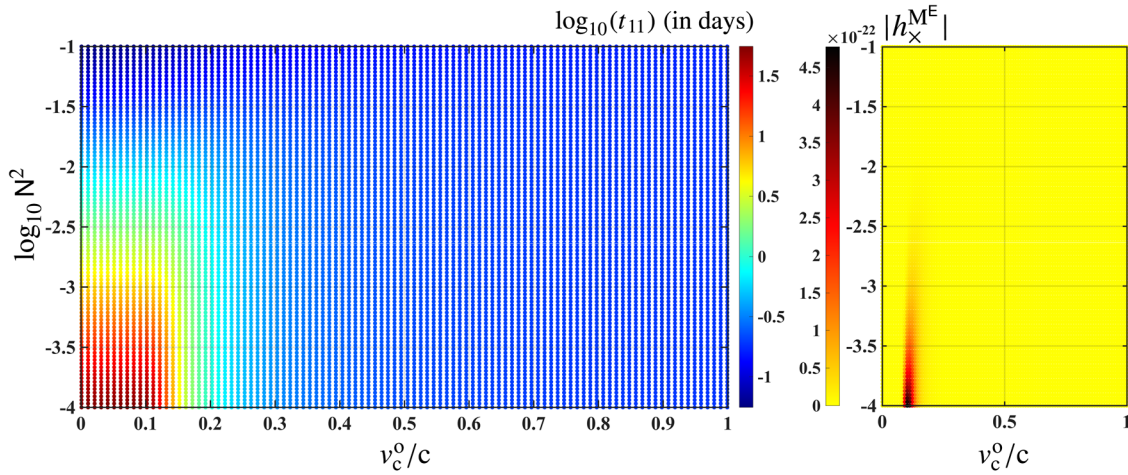


FIG. 6. Sensitivity to E. The characteristics of emitted signals for $E = 10^{-14}$ and $\partial_z v_c = 0$ are shown, setting $f = 100$ Hz, $\epsilon = 10^{-4}$, $d_s = 1$ kpc, $L = 10^4$ m, $g = 10^{12}$ m/sec², $\rho_o = 10^{17}$ kg/m³. Note the emission of loud amplitudes within the range $N^2 \in (10^{-4}, 10^{-2})$; the equivalent classical Brunt-Väisälä frequency N_c^2 for this range lies within permitted physical expectations.

space. In Fig. 5, we show the characteristics in the vicinity of the outlier for clarity.

A. Growing modes

In Fig. 4, for $\partial_z v_c < 0$ (the rightmost panels), we see that it is possible for the system to exhibit *growing modes*. Growing modes refer to the cases where perturbations become unstable and grow monotonically, denoted by the + marker in Figs. 4 and 5. Growing modes are characterized by negative time scales, i.e., $t_{\alpha\gamma} < 0$. In standard oceanography and fluid mechanics literature, growing modes are associated with convection and overturning [29]. They represent a system that gains energy from its surroundings and is not in an adiabatic state. However, this is not true for our system since it is an isolated neutron star. For this reason, these growing modes are unphysical¹⁹ and the corresponding regions in the parameter space are gravitationally inaccessible.

VI. DISCUSSION

To conclude our study, one can broadly make the following reiterations and conclusions. We have extended the previous works by van Eysden and Melatos [5] and Bennett *et al.* [15] by incorporating a more general *equation of state* (characterized by v_c) and *stratification length* (characterized by K_s) in Secs. II and III. We derived the expected time scales of emission of gravitational wave signals and the corresponding strain amplitudes from mass-quadrupole and current-quadrupole formalisms in Sec. IV. In order to better visualize the results, we explored the properties of emission in $\{N^2, v_c^0\}$ parameter space by

making some simplifying approximations given by (81) in Sec. IV C. The results are shown in Fig. 4, where we find that it is possible for such a hydrodynamic system to emit gravitational waves at a ground-based detector with a strain amplitude greater than $O(10^{-25})$ for a source at a distance of roughly 1 kpc. The corresponding time scales for the loudest signals are as long as $O(300)$ days, also shown in Fig. 4. The results in Fig. 4 are explored for favorable values of physical parameters such as at glitch magnitude $\epsilon = O(10^{-4})$, $d_s = 1$ kpc, and $f = 100$ Hz. The analysis yields a strain amplitude as high as $O(10^{-21})$ toward lower magnitudes of N^2 , i.e., $N^2 \leq O(10^{-5})$, and with v_c^0 approximately equaling $0.09c-0.11c$, for the majority of individual amplitudes.²⁰ Besides, in a broader range of values of N^2 and v_c^0 , unlike the aforementioned ranges, we expect emission on the order of $O(10^1 - 10^{1.5})$ days in duration, with amplitudes in the range of $O(10^{-23.5} - 10^{-26.5})$. It must be noted that the current-quadrupole contribution tends to be larger than the corresponding mass-quadrupole contribution to the emitted signal, as shown in Sec. IV and Fig. 4. This is largely because of the characteristic amplitude h_o^C being larger than h_o^M by a factor²¹ of $\frac{2g}{3\Omega c}$. Furthermore, very low values of N^2 (as low as $10^{-6} - 10^{-7}$) are debatable since no physical phenomenon accounts for such magnitudes of N^2 . Note that the “classical” Brunt-Väisälä frequency N_c^2 is expected to lie loosely in the range of $(0.01, 1)$ [5]. The equivalent magnitude of the lower bound on the redefined Brunt-Väisälä frequency N^2 is then given as $N^2 \sim \eta_o N_c^2 = 10^{-4}$ for $v_c^0 = 0.1c$. Thus, very low values of N^2 lie outside the current estimates on equivalent

¹⁹A brief explanation and interpretation of the existence of growing modes is discussed in Sec. H of the Appendix and Sec. VI, respectively.

²⁰See Sec. H of the Appendix for further details.

²¹This factor yields a value of the order $O(10^1-10^2)$ for $\Omega = O(10^2$ Hz), assuming that $g = O(10^{12}$ m/sec²).

values of N_c^2 . In fact, very loud signals of amplitude $O(10^{-25})$ and higher lie near the lower bound of current estimates on N_c^2 , roughly in the range 10^{-4} – 10^{-7} for N^2 . However, the value of Ekman number E could lie anywhere in the range 10^{-17} – 10^{-7} [5,15,21–26,30], whereas we have based our analysis on the assumption of $E = 10^{-7}$. The time scales and the corresponding gravitational wave amplitudes depend on E , such that $E \downarrow \Rightarrow t_{\alpha\gamma} \uparrow \Rightarrow h_R \uparrow$. Thus, for lower values of E , stronger emissions could occur even at higher values of N^2 . This effect is shown in Fig. 6, where we have regenerated parts of Fig. 4 for $E = 10^{-14}$. Note that since the Ekman number is directly proportional to the shear viscosity of the bulk matter [25,31] and inversely proportional to the square of its temperature, we expect higher values of E (10^{-7}) for colder neutron stars ($T \sim 10^6$ K) [26], and vice versa. Thus, in principle, hotter neutron stars should be better candidates for transient gravitational waves than colder neutron stars. However, this is not entirely true since it is expected that hotter and younger neutron stars undergo post-glitch relaxation via crust-core dynamics aided by the magnetic field rather than bulk hydrodynamics [10,32].

A. Detectability of emitted signals

We can also derive characteristics of emitted signals as a function of the rotational frequency f of the neutron star. It has been shown that the minimum strain amplitude h_0^{\min} of a continuous gravitational wave detectable by a network of two detectors searched over a large parameter space with a coherent search duration of T_{obs} hours during which the signal is present is given by [33,34]

$$h_0^{\min}(\omega) = K_t \left[\frac{S_h(\omega)}{T_{\text{obs}}(\omega)} \right]^{\frac{1}{2}}, \quad (83)$$

where $\sqrt{S_h(\omega)}$ is the *multidetector amplitude spectral density* for a network of two detectors (H1, L1), and K_t is roughly equal to 30. Given this relation, we can compare the strength of the emitted gravitational wave signals with the strain detectable by aLIGO. We again restrict ourselves to emission at resonant frequencies only, i.e., $\omega = \omega_R$. Note that we can express h_0^{\min} as a function of f instead of ω since ω_R is an implicit function of f . This allows us to rewrite h_0^{\min} as

$$h_0^{\min}(f) \sim 30.0 \left[\frac{S_h(f)}{t_{\alpha\gamma}(f)} \right]^{\frac{1}{2}}, \quad (84)$$

where $t_{\alpha\gamma}$ is expressed in hours.²² In Fig. 7, we plot $h_0^{\min}(f)$ and compare it with the emitted gravitational wave

²²Refer to Sec. G of the Appendix for a discussion of the properties of $t_{\alpha\gamma}$ as a function of f .

amplitudes²³ as a function of f . We have set the parameters E , v_c^0 , and N^2 at the nominal values 10^{-10} , $0.1c$, and 10^{-4} , respectively. We find that, for the selected region in parameter space in Fig. 7, it is possible to detect the gravitational wave emission with current aLIGO sensitivity, especially in the mid to high frequency range.

One must carefully note that we have assumed an invariant N^2 in space and time in order to simplify our results for easier graphical visualization and understanding. In principle, one could vary all of the featured parameters, i.e., N^2 or K_s , v_c , v_{eq} , in all possible ways. This is because all analytically derived results in Secs. II–IV B are general in nature and assume none of the approximations described in Sec. IV C. However, such a thorough and complete analysis will require extensive numerical computations and better priors on the parameter space. More importantly, the main aim of this study was to estimate the strength of the emitted gravitational wave signals and their time scales as a function of the spatial variation in the adiabatic sound speed v_c and the stratification length z_s . This is shown in detail in Figs. 4 and 5. We find that the signal characteristics are more sensitive to small spatial variations in v_c and K_s in some regions of parameter space than others. In fact, for these regions in parameter space, the maximum duration of the emission increases by a factor of 300 when $\partial_z v_c = -10^{-4} cL^{-1}$, as compared to when $\partial_z v_c = 0$. The corresponding amplitudes also increase by a similar factor, as seen in Figs. 4 and 5. In parts of the parameter space characterized by growing modes, no gravitational emission is possible due to hydrodynamic instability.

B. Energetics of the system

It is an interesting exercise to estimate the fraction of mechanical energy (from the glitch) that gets converted into gravitation wave emission. For instance, the total gravitational wave energy emitted by a waveform $h(t) \propto e^{i\Omega_w t} e^{-\gamma_w t}$ is given by [27,35]

$$E_{\text{GW}} = \frac{c^3}{8G} [\Omega_w^2 + \gamma_w^2] d_s^2 \int_0^\infty |h(\omega)|^2 d\omega, \quad (85)$$

where we have used Parseval's theorem such that

²³Note that the resonant frequencies of the emitted modes for the mass-quadrupole and current-quadrupole contributions, and for a given orientation of the observer (polar, equatorial, or otherwise), depend on the polarizations (+ and \times), which in turn depend on the featured time scales $t_{\alpha\gamma}$, as seen in Fig. 4 and Sec. IV. The overall signal is a superposition of all such individual emissions shown in Fig. 7, possibly at multiple resonant frequencies for a single source with a given orientation. In this regard, (84) assumes that these individual emissions are resolvable in frequency; this usually holds true when the featured time scales $t_{\alpha\gamma}$ are not very small (see Secs. IV A and IV B).

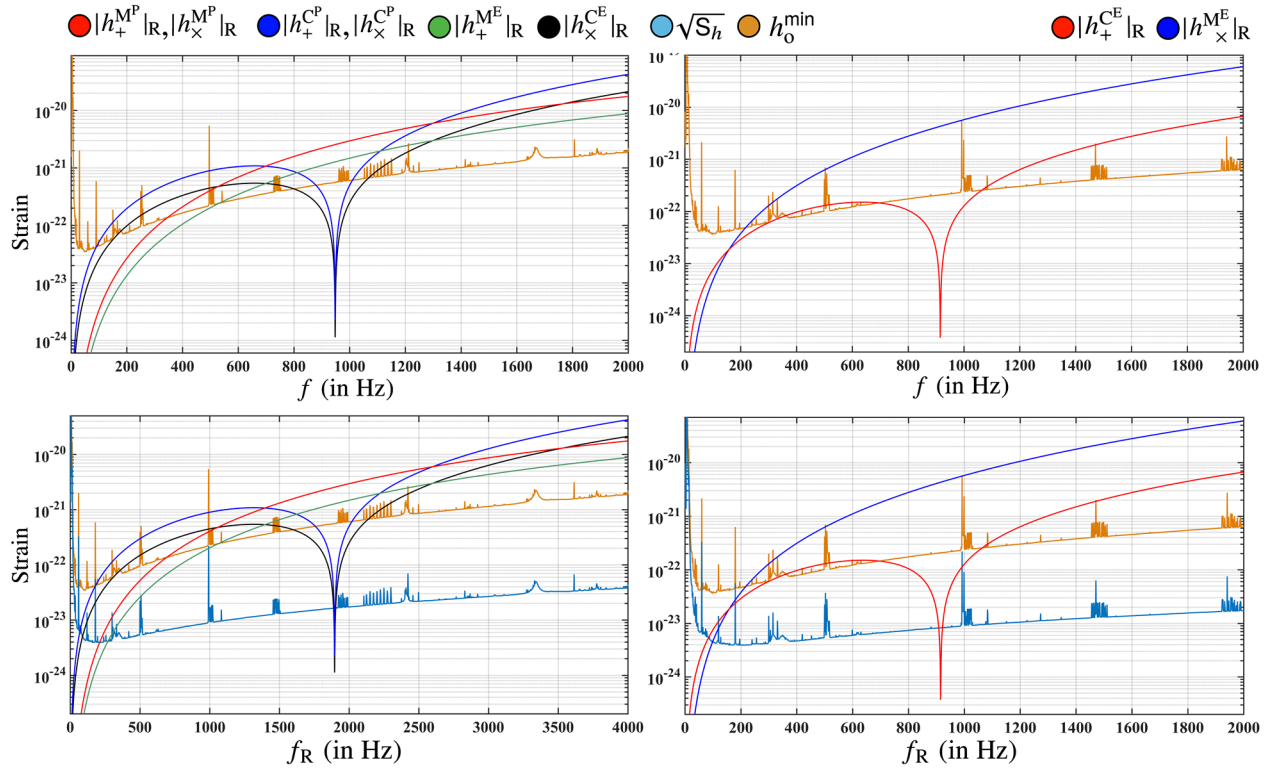


FIG. 7. Sensitivity vs f . The characteristics of emitted signals²⁴ and h_0^{\min} are shown as a function of the neutron star's rotational frequency f as well as the emitted resonant frequency f_R , given as $f_R = \omega_R/2\pi$. We have set $v_c^0 = 0.1c$, $N^2 = 10^{-4}$, $E = 10^{-10}$, $\epsilon = 10^{-4}$, $d_s = 1$ kpc, $L = 10^4$ m, $g = 10^{12}$ m/sec², $\rho_0 = 10^{17}$ kg/m³, $\partial_z v_c = 0$. Note that the emitted amplitudes are largely insensitive to $\partial_z v_c$ for the chosen points in $\{v_c^0, N^2\}$ parameter space. The multidetector amplitude spectral density $\sqrt{S_h(\omega)}$ is calculated by taking the harmonic mean of the individual amplitude spectral densities of the H1 (aLIGO Hanford) and L1 detectors (aLIGO Livingston) measured during initial days of the O1 run, i.e., September 12 through October 20, 2015.

$$\int_0^\infty |h(t)|^2 dt = \frac{1}{2\pi} \int_0^\infty |h(\omega)|^2 d\omega. \quad |h(\omega)|^2 \sim 2 \sum_{\mathcal{P}=+,x} \left[\sum_{\mathcal{L}=M,C} |h_{\mathcal{P}}^{\mathcal{L}}(\omega)| \right]^2. \quad (86)$$

We can easily calculate E_{GW} by integrating (numerically or analytically) the total emitted waveform²⁴ over time, or by integrating its Fourier transform in frequency space. Note that expression (85) assumes an isotropic distribution of signal as a function of the observation angle i . In our case, the emission is not isotropically distributed as a function of i . In fact, the amplitude for a given polarization varies as a linear combination of sines and cosines of i , as briefly discussed in Sec. D of the Appendix [15]. In order to simplify this to an order-of-magnitude estimate, the total emission can be constrained by an isotropic limit, such that²⁵

²⁴Note that the total emission is a sum of the mass-quadrupole and current-quadrupole emission.

²⁵This approximation assumes that the amplitude measured by a polar observer is isotropically distributed as a function i . This is a reasonable assumption for an order-of-magnitude estimate of the emitted energy considering that the observed amplitudes for polar and equatorial observers are of the same order of magnitude, as seen in Figs. 2, 3, and 7.

Combining (85) and (86), we get

$$E_{\text{GW}} \sim \frac{c^3}{4G} [\Omega_w^2 + \gamma_w^2] d_s^2 \int_0^\infty \sum_{\mathcal{P}=+,x} \left[\sum_{\mathcal{L}=M,C} |h_{\mathcal{P}}^{\mathcal{L}}(\omega)| \right]^2 d\omega. \quad (87)$$

On the other hand, the total mechanical energy E_{glitch} imparted by the glitch is written as²⁶

$$E_{\text{glitch}} \sim \Gamma M_{\text{total}} L^2 \Omega_r \Delta \Omega_r = 2\pi \epsilon \Gamma \rho_0 L^5 \Omega_r^2, \quad (88)$$

where Γ is the fraction of total neutron star mass ($M_{\text{total}} \sim 2\pi\rho_0 L^3$) contained within the crust; this is

²⁶This approximation assumes that only the crust of the neutron star gains angular momentum from the glitch, while the bulk fluid is decoupled from the crust at the time of the glitch. Moreover, we also assume that the crust is very thin compared to the radius of the cylinder, and it contains only a fraction of the mass [$O(10^{-2})$] of the entire neutron star.

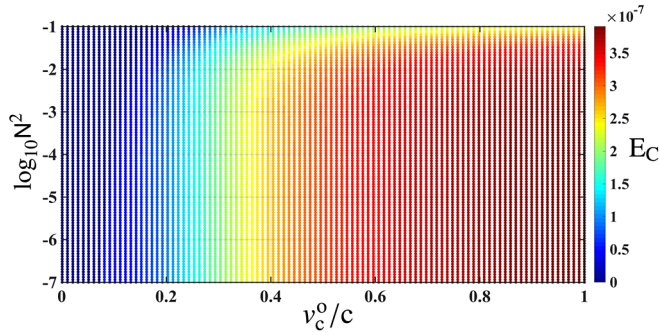


FIG. 8. Energetics. We have set $E = 10^{-7}$, $\epsilon = 10^{-4}$, $d_s = 1$ kpc, $L = 10^4$ m, $g = 10^{12}$ m/sec², $\rho_o = 10^{17}$ kg/m³, and $\partial_z v_c = 0$. We find that similar results, i.e., $E_C = O(10^{-7})$, are achieved when we set $0 < |\partial_z v_c| \ll 1$; this is due to the fact that $\kappa_{\alpha\gamma}$ and $V_{\alpha\gamma}$ show very weak dependence on $\partial_z v_c$ when $|\partial_z v_c| \ll 1$.

assumed to be a small fiducial value of 10^{-2} . Then the fraction of mechanical energy $E_C (= E_{\text{GW}}/E_{\text{glitch}})$ converted into gravitational waves is given as

$$E_C \sim \frac{c^3}{8\pi G} \frac{[\Omega_w^2 + \gamma_w^2] d_s^2}{e\Gamma\rho_o L^5 \Omega_r^2} \int_0^\infty \sum_{\mathcal{P}=\pm, \times} \left[\sum_{\mathcal{L}=\text{M,C}} |h_{\mathcal{P}}^{\mathcal{L}}(\omega)| \right]^2 d\omega. \quad (89)$$

We find that the ratio E_C yields values on the order of $O(10^{-7})$, assuming $\Omega_w \sim 2\Omega_r$. This suggests that a large fraction of the energy from the glitch is converted into the kinetic and potential energy of the bulk fluid. We also note that the value of E_C in the $\{N^2, v_c^0, \partial_z v_c\}$ parameter space depends only on the prefactors $\kappa_{\alpha\gamma}$ and $V_{\alpha\gamma}$.²⁷ In Fig. 8, we show an example of the characteristics of E_C .

C. Choice of equation of state

In (4), we assumed a simple form of the equation of state where the adiabatic speed of sound v_c is slowly and linearly varying with z . It may be useful to compare this choice with a general polytropic equation of state with polytropic index n , polytropic exponent $\gamma = (n+1)/n$, and polytropic constant K_p , i.e., $p = K_p \rho^\gamma$. The adiabatic speed of sound v_p for the polytropic equation is given as $v_p^2 = K_p \rho^{1/n}$. Clearly, our model of equation of state resembles the polytropic model for $n \rightarrow \infty$. We also know that neutron star interiors are generally well modeled for values of the polytropic index $n \in (0.5, 1.5)$. Thus, we should inquire whether our assumption of $n \rightarrow \infty$ is reasonable. In order to answer this question, consider that the gravitational wave emission is almost entirely dominated by the processes occurring at the viscous boundary layer, such as the

²⁷Note that this dependence is generally biased toward $V_{\alpha\gamma}$ since the current-quadrupole emission is significantly louder than the mass-quadrupole emission.

exchange of fluid across this layer, as discussed in great detail in Secs. A 8, A 1, and III H. These processes determine the time scales of relaxation, which in turn determine the peak gravitational wave amplitudes (at resonant frequencies). We also note that the prefactors $\kappa_{\alpha\gamma}$ and $V_{\alpha\gamma}$ are largely insensitive to these processes, as discussed in Sec. VI B. Thus, our choice of equation of state particularly encodes physical processes at the viscous boundary layer. In the vicinity of this viscous boundary layer, i.e., $z \sim 1$, any polytropic equation of state can be reduced to linear order in z . In this limit, the true form of the equation of state becomes irrelevant. For example, for an $n = 1$ polytrope,

$$v_p|_{z \sim 1} = \sqrt{K_p \rho|_{z \sim 1}} \sim v_c^0 + \partial_z v_c. \quad (90)$$

Specifically, for a typical crust density of $\rho|_{z \sim 1} \sim 10^9$ kg m⁻³, $v_c^0 \sim c$, and $\partial_z v_c \sim 0$, we find that $K_p \sim 10^7$ kg⁻¹ m⁵ s⁻².

However, there are certain aspects that we have overlooked, such as the effects of the magnetic field and the superfluid nature of the core. The strong magnetic field in neutron stars affects the crust-core interactions and coupling dynamics of the superfluid [10,32], possibly shortening the duration of the emission, especially in young and hot neutron stars such as the Vela pulsar [36]. Recent works by van Eysden [37] have explored the effect of the magnetic field on the post-glitch relaxation phase, but in a slightly different context. Note that we have assumed that non-axisymmetric modes are equally likely to be excited by the glitch as the axisymmetric ones ($C_\alpha = 1$). If this assumption does not hold, the gravitational amplitudes should be rescaled by the same factor. In conclusion, we believe this to be a viable model to predict the expected order of magnitude of the amplitude and duration of the emitted gravitational wave signals from glitching neutron stars that involve relaxation via Ekman pumping. It lays down a basic approach for predicting the approximate internal state of the neutron star and first-order variations in it, if any such transient signal is detected by gravitational wave detectors from the post-glitch relaxation phase.

ACKNOWLEDGMENTS

I would like to extend my hearty thanks to Maria Alessandra Papa at the Max-Planck-Institut für Gravitationsphysik for her support throughout, and to Andrew Melatos for his input through the course of this work.

APPENDIX

1. Time evolution

In this section, we derive the time evolution of the $\chi(r, \phi, z, t)$ function. We begin by isolating the time

dependence in $\chi(r, \phi, z, t)$ by separating the variables as follows:

$$\chi(r, \phi, z, t) \equiv \bar{\chi}(r, \phi, z) T(t). \quad (\text{A1})$$

In parallel, we take the time derivative of (42),

$$\begin{aligned} \partial_t(\delta v_z)|_{z=\pm 1} &= \mp \frac{1}{2} E^{\frac{1}{2}} \partial_t(\nabla \times \delta \vec{v})_z|_{z=\pm 1} \\ &= \pm \frac{1}{2} E^{\frac{1}{2}} \left[\frac{1}{r} \frac{\partial}{\partial r} (r \partial_t[\delta v_\phi]) - \frac{1}{r} \frac{\partial}{\partial \phi} (\partial_t[\delta v_r]) \right] \Big|_{z=\pm 1}. \end{aligned} \quad (\text{A2})$$

Ignoring all the $O(E^1)$ or higher-order terms on the right-hand side of (A2) and using results from Secs. III D and III E and (44), we get

$$\begin{aligned} \partial_t[\delta v_z^{(1)}]|_{z=\pm 1} &= \mp \frac{1}{4F} \left[\frac{1}{r^2} \frac{\partial^2 \chi}{\partial \phi^2} + \frac{1}{r} \frac{\partial}{\partial r} \left(r \frac{\partial \chi}{\partial r} \right) \right] \Big|_{z=\pm 1} \\ &= \pm \frac{1}{4F} \lambda_{\alpha\gamma}^2 \chi \Big|_{z=\pm 1}. \end{aligned} \quad (\text{A3})$$

Moreover, we use (39) to further simplify (A3) as

$$\left[\frac{\eta(z)}{FN^2(z)} \frac{\partial \dot{\chi}}{\partial z} + \left\{ \frac{-\partial_z \eta}{FN^2(z)} - 1 \right\} \dot{\chi} \right] \Big|_{z=\pm 1} = \mp \frac{1}{4F} \lambda_{\alpha\gamma}^2 \chi \Big|_{z=\pm 1}. \quad (\text{A4})$$

Now, introducing the separation of variables from (A1), we rewrite the above equation (A4) as

$$\begin{aligned} \left[\frac{\eta(z)}{FN^2(z)} \frac{\partial \bar{\chi}}{\partial z} + \left\{ \frac{-\partial_z \eta}{FN^2(z)} - 1 \right\} \bar{\chi} \right] \Big|_{z=\pm 1} \dot{T}(t) \\ = \mp \frac{1}{4F} \lambda_{\alpha\gamma}^2 \bar{\chi} \Big|_{z=\pm 1} T(t). \end{aligned} \quad (\text{A5})$$

We further reduce the previous expression (A5) by separating the variables into (r, ϕ) and z to

$$\begin{aligned} \left[\frac{\eta(\pm 1)}{FN^2(\pm 1)} \frac{\partial Z_{\alpha\gamma}}{\partial z} \Big|_{z=\pm 1} + \left\{ \frac{-\partial_z \eta|_{z=\pm 1}}{FN^2(\pm 1)} - 1 \right\} \times Z_{\alpha\gamma}(\pm 1) \right] \dot{T}(t) \\ = \mp \frac{1}{4F} \lambda_{\alpha\gamma}^2 Z_{\alpha\gamma}(\pm 1) T(t). \end{aligned} \quad (\text{A6})$$

Equation (A6) can now be solved to yield $T(t)$ as

$$T(t) \propto e^{-\omega_{\alpha\gamma} t}, \quad (\text{A7})$$

such that $\omega_{\alpha\gamma}$ is given as

$$\begin{aligned} \omega_{\alpha\gamma} &= \frac{1}{4F} \lambda_{\alpha\gamma}^2 Z_{\alpha\gamma}(1) \left[\frac{\eta(1)}{FN^2(1)} \frac{\partial Z_{\alpha\gamma}}{\partial z} \Big|_{z=1} \right. \\ &\quad \left. + \left\{ \frac{-\partial_z \eta|_{z=1}}{FN^2(1)} - 1 \right\} Z_{\alpha\gamma}(1) \right]^{-1}. \end{aligned} \quad (\text{A8})$$

Note that $Z_{\alpha\gamma}(z)$ is symmetric about the $z = 0$ plane and we have evaluated the expression at $z = 1$.

2. Bessel-Fourier coefficients

In this section, we will calculate the Bessel-Fourier coefficients introduced in (52). We use the *orthogonality property* of the Bessel functions, which states that Bessel functions are orthogonal with respect to the inner product, as follows²⁸:

$$\begin{aligned} \langle J_\alpha(\lambda_{\alpha\gamma} r), J_\alpha(\lambda_{\alpha\alpha} r) \rangle &= \int_0^1 r J_\alpha(\lambda_{\alpha\gamma} r) J_\alpha(\lambda_{\alpha\alpha} r) dr \\ &= \frac{1}{2} \delta_{\gamma\alpha} [J_{\alpha+1}(\lambda_{\alpha\gamma} r)]^2. \end{aligned} \quad (\text{A9})$$

For a Fourier-Bessel series of the form $f(r) = \sum_{\alpha=1}^{\infty} C_\alpha J_\alpha(\lambda_{\alpha\alpha} r)$, the coefficients C_α can be calculated by taking projection of the function $f(r)$ over the corresponding Bessel functions as

$$C_\alpha = \frac{\langle f(r), J_\alpha(\lambda_{\alpha\alpha} r) \rangle}{\langle J_\alpha(\lambda_{\alpha\gamma} r), J_\alpha(\lambda_{\alpha\gamma} r) \rangle}. \quad (\text{A10})$$

Using the above relation in combination with (53), we can substitute for $f(r)$,

$$\begin{aligned} f(r) &= \delta P_0 - \delta P_\infty = \sum_{\alpha=0}^{\infty} \sum_{\gamma=1}^{\infty} \omega_{\alpha\gamma}^{-1} J_\alpha(\lambda_{\alpha\gamma} r) \times [A_{\alpha\gamma} \cos(\alpha\phi) \\ &\quad + B_{\alpha\gamma} \sin(\alpha\phi)] Z_{\alpha\gamma}(z) \\ &= \left[\sum_{\alpha=0}^{\infty} C_\alpha r^\alpha (r^2 - 1) \cos(\alpha\phi) Z_{\alpha\gamma}(z) \right] - r^2, \end{aligned} \quad (\text{A11})$$

which, when applied to (A10), gives

$$\begin{aligned} \omega_{\alpha\gamma}^{-1} A_{\alpha\gamma} \cos(\alpha\phi) Z_{\alpha\gamma}(z) \\ = \frac{2}{J_{\alpha+1}^2(\lambda_{\alpha\gamma})} \int_0^1 r \times J_\alpha(\lambda_{\alpha\gamma} r) [\delta P_0 - \delta P_\infty] dr. \end{aligned} \quad (\text{A12})$$

We multiply both sides by $\cos(\alpha\phi)$ and integrate the resulting expression in the ϕ and z variables, assuming that $A_{\alpha\gamma}$ is an absolute constant, and arrive at the following result:

²⁸ $\delta_{\gamma\alpha}$ is the Dirac-delta function.

$$A_{\alpha\gamma} = \frac{2\omega_{\alpha\gamma}}{\pi J_{\alpha+1}^2(\lambda_{\alpha\gamma})} \int_0^{2\pi} d\phi \int_0^1 dz \int_0^1 r dr \\ \times J_\alpha(\lambda_{\alpha\gamma} r) \cos(\alpha\phi) [\delta P_0 - \delta P_\infty] Z_{\alpha\gamma}^{-1}(z). \quad (\text{A13})$$

Similarly, for $B_{\alpha\gamma}$,

$$B_{\alpha\gamma} = \frac{2\omega_{\alpha\gamma}}{\pi J_{\alpha+1}^2(\lambda_{\alpha\gamma})} \int_0^{2\pi} d\phi \int_0^1 dz \int_0^1 r dr \\ \times J_\alpha(\lambda_{\alpha\gamma} r) \sin(\alpha\phi) [\delta P_0 - \delta P_\infty] Z_{\alpha\gamma}^{-1}(z). \quad (\text{A14})$$

3. Quadrupole moment formalism

In this section, we will underline the formalism for calculating expressions (62)–(71) for gravitational wave emission. In the reference frame of a polar observer at a distance d , the components of the gravitational wave strain in Einstein's quadrupole moment formalism in the transverse traceless (TT) gauge are given as

$$h_+(t) = h_{xx}^{\text{TT}}(t) = -h_{yy}^{\text{TT}}(t) = \frac{G}{c^4 d} [\ddot{I}_{xx}(t) - \ddot{I}_{yy}(t)], \quad (\text{A15})$$

$$h_\times(t) = h_{xy}^{\text{TT}}(t) = \frac{2G}{c^4 d} \ddot{I}_{xy}(t), \quad (\text{A16})$$

where $I_{ik}(t)$ is the reduced quadrupole moment of inertia, and it is given in terms of the stress-energy tensor component T^{00} as

$$I_{ik}(t) = \frac{1}{c^2} \int d^3\vec{x} \left[x_i x_k - \delta_{ik} \frac{|\vec{x}|^2}{3} \right] T^{00}(\vec{x}, t). \quad (\text{A17})$$

Combining (A15), (A16), and (A17), we get

$$h_+^{\text{P}}(t) = \frac{G}{c^6 d} \int d^3\vec{x} [x^2 - y^2] \ddot{T}^{00}(\vec{x}, t) \\ = \frac{G}{c^6 d} \int d^3\vec{r} r^2 \cos(2\phi) \ddot{T}_{\text{NA}}^{00}(\vec{r}, t), \quad (\text{A18})$$

$$h_\times^{\text{P}}(t) = \frac{2G}{c^6 d} \int d^3\vec{x} [xy] \ddot{T}^{00}(\vec{x}, t) \\ = \frac{G}{c^6 d} \int d^3\vec{r} r^2 \sin(2\phi) \ddot{T}_{\text{NA}}^{00}(\vec{x}, t), \quad (\text{A19})$$

where the subscript NA refers to nonaxisymmetric terms. Moreover, in the case of a perfect fluid, we neglect the viscous terms while evaluating $T^{\mu\nu}$ since they are of the order $O(\epsilon)$, and the stress-energy tensor component T^{00} is then given as

$$T^{00} = \left[\rho + \frac{p}{c^2} \right] u^0 u^0 + p g^{00}, \quad (\text{A20})$$

where the 0-component u^0 of the 4-velocity \vec{u} is given as

$$u^0 = \frac{c}{\sqrt{1 - \frac{\vec{v} \cdot \vec{v}}{c^2}}}. \quad (\text{A21})$$

We break expression (A20) into separate terms describing the constitutive equilibrium and perturbative terms, i.e., $\rho \rightarrow \rho_e + \epsilon \delta \rho$, $p \rightarrow p_e + \epsilon \delta p$ and $\vec{v} \rightarrow \vec{v}_r + \delta \vec{v}$, as described in Sec. III B. Here, \vec{v}_r is simply the velocity of a fluid element given in cylindrical coordinates as $\vec{v}_r = (0, \Omega r, 0)$, assuming corotation with the neutron star crust. Note that the equilibrium state is axisymmetric in nature and does not contribute to the signal emission. The contributing nonaxisymmetric terms in T^{00} are then given as²⁹

$$T_{\text{NA}}^{00} = \epsilon \delta \rho c^2 + (\rho_e c^2 + p_e) \left[2 \frac{\delta \vec{v} \cdot \vec{v}_r}{c^2} + \frac{\delta \vec{v} \cdot \delta \vec{v}}{c^2} \right] \\ + \epsilon (\delta \rho c^2 + \delta p) \left[2 \frac{\delta \vec{v} \cdot \vec{v}_r}{c^2} + \frac{\vec{v}_r \cdot \vec{v}_r}{c^2} + \frac{\delta \vec{v} \cdot \delta \vec{v}}{c^2} \right] \\ \sim \epsilon \delta \rho c^2 + (\rho_e c^2 + p_e) \left[2 \frac{\delta \vec{v} \cdot \vec{v}_r}{c^2} + \frac{\delta \vec{v} \cdot \delta \vec{v}}{c^2} \right] \\ + (\epsilon \delta \rho c^2 + \delta p) \left[\frac{\vec{v}_r \cdot \vec{v}_r}{c^2} \right]. \quad (\text{A22})$$

Note that there exists no explicit factor of ϵ when it comes to $\delta \vec{v}$, as discussed previously in Sec. III B. The factor of ϵ in the order of magnitude of $\delta \vec{v}$ is implicitly contained within $\delta \vec{v}$. Furthermore, combining expressions (A18), (A19), and (A22), we calculate the gravitational wave emission up to the order $O(\epsilon^1)$ given by (62)–(71).

4. Current-quadrupole moment

In this section, we briefly describe the method for deriving strain amplitude for the current-quadrupole contribution quoted in (72)–(76). We follow [15,27,28], and make appropriate modifications corresponding to our assumption of spatially varying the stratification length and adiabatic sound speed. The general expression for the + and \times polarizations contributed by the current-quadrupole moment (labeled with the superscript C) for a general observer at distance d is given as [15,27,28]

$$h_+^{\text{C}}(t) = \frac{G}{2c^5 d} \left[\frac{5}{2\pi} \right]^{\frac{1}{2}} [\text{Im}\{\ddot{C}^{21}(t)\} \sin(i) \\ + \text{Im}\{\ddot{C}^{22}(t)\} \cos(i)], \quad (\text{A23})$$

$$h_\times^{\text{C}}(t) = \frac{G}{4c^5 d} \left[\frac{5}{2\pi} \right]^{\frac{1}{2}} [\text{Re}\{\ddot{C}^{21}(t)\} \sin(2i) \\ + \text{Re}\{\ddot{C}^{22}(t)\} [1 + \cos^2(i)]], \quad (\text{A24})$$

²⁹Here, we have assumed $g^{00} = -1$ and $|v^2| \ll c^2$.

where $C^{l\nu}(t)$ represents the (l, ν) multipoles of the mass-current distribution. Note that we have only considered the leading-order quadrupole moment ($l = 2$), which is the lowest multipole moment that contributes to the gravitational wave emission via its nonvanishing second-order time derivative $\ddot{C}^{2\nu}(t)$. The presence of an additional c^5 factor, as opposed to c^4 in the case of the mass-quadrupole moment, suggests that the current-quadrupole contribution is much smaller than the mass-quadrupole moment. This is true for systems with low density. However, for high-density systems such as a neutron star, current-quadrupole emission may be larger than the mass-quadrupole contribution, as described in Sec. IV B. We have also ignored the $\nu = 0$ mode, which contributes at the order of $O(E^1)$ while retaining the more significant $\nu = 1, 2$ modes. Moreover, i denotes the angle between the neutron star's rotation axis and the observer's line of sight, such that $i = 0$ for a polar observer, and $i = 90^\circ$ for an equatorial observer. The $C^{2\nu}(t)$ terms are explicitly given as [15]³⁰

$$C^{2\nu}(t) = \frac{(-1)^{\nu+1} 8\pi (10\pi)^{\frac{1}{2}}}{15\nu\rho_0^{-1} L^{-6} (\delta\Omega)^{-1}} \sum_{\gamma=1}^{\infty} V_{\nu\gamma} e^{-(E^{\frac{1}{2}}\omega_{\nu\gamma} + i\nu)\Omega t}, \quad (\text{A25})$$

where

$$V_{\nu\gamma} = 2A_{\nu\gamma}\omega_{\nu\gamma}^{-1} \int_0^1 dr \int_0^1 dz r^{\nu+1} z^{2-\nu} \times \hat{\mathbf{U}}[J_\nu(\lambda_{\nu\gamma}r)Z_{\nu\gamma}(z)\rho_e(z)]. \quad (\text{A26})$$

Moreover, the operator $\hat{\mathbf{U}}$ is written as

$$\hat{\mathbf{U}} = \left[z \frac{\partial^2}{\partial r^2} + \frac{z}{r} \frac{\partial}{\partial r} - z \frac{\nu^2}{r^2} - r \frac{\partial^2}{\partial r \partial z} \right] + 2F \left[r^2 \frac{\partial^2}{\partial z^2} - rz \frac{\partial^2}{\partial r \partial z} - 2z \frac{\partial}{\partial z} \right]. \quad (\text{A27})$$

Finally, the expressions for the $+$ and \times polarizations can now be reduced using the above relations to the expressions quoted in (72)–(76).

5. $\kappa_{\nu\gamma}$ and $V_{\nu\gamma}$

In this section, we quote the full expression of $\kappa_{\nu\gamma}$ ³¹:

$$\begin{aligned} \kappa_{\nu\gamma} = & 2\omega_{\nu\gamma}^{-1} A_{\nu\gamma} \left[\int_0^1 dr r^3 J_\nu(\lambda_{\nu\gamma}r) \int_0^1 dz \partial_z [-Z_{\nu\gamma}(z)\rho_e(z)] + K \int_0^1 dr r^4 \partial_r [J_\nu(\lambda_{\nu\gamma}r)] \right. \\ & \left. \times \int_0^L dz \left[1 + \frac{K}{K_s(z)} \right] Z_{\nu\gamma}(z)\rho_e(z) + \frac{\Omega^2 L^2}{c^2} \int_0^1 dr r^5 J_\nu(\lambda_{\nu\gamma}r) \int_0^1 dz [\partial_z [-Z_{\nu\gamma}(z)\rho_e(z)] + K Z_{\nu\gamma}(z)\rho_e(z)] \right]. \quad (\text{A28}) \end{aligned}$$

Moreover, following the assumptions described in (81) in Sec. IV C, the above expression for $\kappa_{\nu\gamma}$ can be further reduced to a simpler and easier form. The simplifying assumptions lead to the case where all coefficients in (46) become effectively invariant with respect to the z coordinate. This makes the solution for $Z_{\nu\gamma}(z)$ straightforward to achieve. Moreover, the integrals in the exponents involving K_s in (A28) are dissolved, and the resulting exponential terms can be folded into $Z_{\nu\gamma}(z)$ to yield

$$\kappa_{\nu\gamma} = 2\omega_{\nu\gamma}^{-1} A_{\nu\gamma} \left[\mathcal{L}_1 \int_0^1 dr r^3 J_\nu(\lambda_{\nu\gamma}r) + K \left[1 + \frac{K}{K_s} \right] \mathcal{L}_2 \int_0^1 dr r^4 \partial_r [J_\nu(\lambda_{\nu\gamma}r)] + \frac{\Omega^2 L^2}{c^2} [\mathcal{L}_1 + K\mathcal{L}_2] \int_0^1 dr r^5 J_\nu(\lambda_{\nu\gamma}r) \right], \quad (\text{A29})$$

where \mathcal{L}_1 and \mathcal{L}_2 are given in terms of \mathcal{K}_\pm as

$$\mathcal{L}_1 = \frac{(\text{FN}^2 - \mathcal{K}_-)[1 - e^{-\mathcal{K}_-}] - (\text{FN}^2 - \mathcal{K}_+)[1 - e^{-\mathcal{K}_+}]}{(\text{FN}^2 - \mathcal{K}_-)e^{\mathcal{K}_+} - (\text{FN}^2 - \mathcal{K}_+)e^{\mathcal{K}_-}}, \quad (\text{A30})$$

³⁰In the case of the current-quadrupole contribution, it is possible to have continuous emission of gravitational waves at large time scales, $t \gg t_{2\nu}$, as shown by Bennett *et al.* [15]. This continuous residual emission is not artificial (cf. van Eysden and Melatos [5]). In calculating the expression for $C^{2\nu}(t)$, we have ignored terms responsible for this residual continuous contribution since we concern ourselves solely with transient emission.

$$\mathcal{L}_2 = \frac{(\text{FN}^2 - \mathcal{K}_-) \frac{1 - e^{-\mathcal{K}_-}}{\mathcal{K}_-} - (\text{FN}^2 - \mathcal{K}_+) \frac{1 - e^{-\mathcal{K}_+}}{\mathcal{K}_+}}{(\text{FN}^2 - \mathcal{K}_-)e^{\mathcal{K}_+} - (\text{FN}^2 - \mathcal{K}_+)e^{\mathcal{K}_-}}. \quad (\text{A31})$$

Furthermore, \mathcal{K}_\pm in (A30) and (A31) is given as

$$\mathcal{K}_\pm = \frac{1}{2} [K_s \pm (K_s^2 + \eta_0^{-1} [N^2 \lambda_{\nu\gamma}^2 + \partial_z \eta - \partial_z^2 \eta])^{\frac{1}{2}}], \quad (\text{A32})$$

where $\eta_0 = (v_0^0/c)^2$, $\partial_z \eta \sim 2v_0^0 \partial_z v_c$, and $\partial_z^2 \eta \sim 2(\partial_z v_c)^2$. Similarly, we calculate the reduced expression for $V_{\nu\gamma}$ in

³¹The prefactor of 2 in $\kappa_{\nu\gamma}$ comes from extending the symmetric integral to $z \in [-1, 1]$.

terms of $\mathcal{L}_3^{(g)}$, $\mathcal{L}_4^{(g)}$, and $\mathcal{L}_5^{(g)}$. We define $\mathcal{L}_3^{(g)}$, $\mathcal{L}_4^{(g)}$, and $\mathcal{L}_5^{(g)}$ as follows:

$$\mathcal{L}_3^{(g)} = \frac{(\text{FN}^2 - \mathcal{K}_-) \mathcal{H}_g(\mathcal{K}_-) - (\text{FN}^2 - \mathcal{K}_+) \mathcal{H}_g(\mathcal{K}_+)}{(\text{FN}^2 - \mathcal{K}_-) e^{\mathcal{K}_+} - (\text{FN}^2 - \mathcal{K}_+) e^{\mathcal{K}_-}}, \quad (\text{A33})$$

$$\mathcal{L}_4^{(g)} = \frac{(\text{FN}^2 - \mathcal{K}_-) \frac{\mathcal{H}_g(\mathcal{K}_-)}{\mathcal{K}_-^{-1}} - (\text{FN}^2 - \mathcal{K}_+) \frac{\mathcal{H}_g(\mathcal{K}_+)}{\mathcal{K}_+^{-1}}}{(\text{FN}^2 - \mathcal{K}_-) e^{\mathcal{K}_+} - (\text{FN}^2 - \mathcal{K}_+) e^{\mathcal{K}_-}}, \quad (\text{A34})$$

$$\mathcal{L}_5^{(g)} = \frac{(\text{FN}^2 - \mathcal{K}_-) \frac{\mathcal{H}_g(\mathcal{K}_-)}{\mathcal{K}_-^{-2}} - (\text{FN}^2 - \mathcal{K}_+) \frac{\mathcal{H}_g(\mathcal{K}_+)}{\mathcal{K}_+^{-2}}}{(\text{FN}^2 - \mathcal{K}_-) e^{\mathcal{K}_+} - (\text{FN}^2 - \mathcal{K}_+) e^{\mathcal{K}_-}}, \quad (\text{A35})$$

where $\mathcal{H}_g(\mathcal{K}_\pm)$ is defined by the integral given below,³²

$$\mathcal{H}_g(\mathcal{K}_\pm) = \int_0^1 dz z^g e^{-\mathcal{K}_\pm z}. \quad (\text{A36})$$

The resulting complete expression for $V_{\nu\gamma}$ is then expanded and written in terms of $\mathcal{L}_3^{(g)}$, $\mathcal{L}_4^{(g)}$, and $\mathcal{L}_5^{(g)}$, as follows:

$$\begin{aligned} V_{\nu\gamma} = & 2A_{\nu\gamma} \omega_{\nu\gamma}^{-1} \left[\mathcal{L}_3^{(3-\nu)} \int_0^1 dr r^{\nu-1} [r^2 \partial_r^2 [J_\nu(\lambda_{\nu\gamma} r)] + r \partial_r [J_\nu(\lambda_{\nu\gamma} r)] - \nu^2 J_\nu(\lambda_{\nu\gamma} r)] + \mathcal{L}_4^{(2-\nu)} \int_0^1 dr r^{\nu+2} \partial_r [J_\nu(\lambda_{\nu\gamma} r)] \right. \\ & \left. + 2F \left[\mathcal{L}_5^{(2-\nu)} \int_0^1 dr r^{\nu+3} J_\nu(\lambda_{\nu\gamma} r) + \mathcal{L}_4^{(3-\nu)} \int_0^1 dr r^{\nu+1} [r \partial_r [J_\nu(\lambda_{\nu\gamma} r)] + 2J_\nu(\lambda_{\nu\gamma} r)] \right] \right]. \quad (\text{A37}) \end{aligned}$$

Moreover, the approximated analytic expression of $t_{\nu\gamma}$ can also be calculated following (81), and it is given as

$$t_{\nu\gamma} = \frac{4E^{-\frac{1}{2}} \Omega^{-1} \text{FN}^2 \text{N}^2 [(\text{FN}^2 - \mathcal{K}_-) e^{\mathcal{K}_+} - (\text{FN}^2 - \mathcal{K}_+) e^{\mathcal{K}_-}]}{\lambda_{\nu\gamma}^2 [(\eta_1 \mathcal{K}_+ - \partial_z \eta|_{z=1} - \text{FN}^2)(\text{FN}^2 - \mathcal{K}_-) e^{\mathcal{K}_+} - (\eta_1 \mathcal{K}_- - \partial_z \eta|_{z=1} - \text{FN}^2)(\text{FN}^2 - \mathcal{K}_+) e^{\mathcal{K}_-}]}, \quad (\text{A38})$$

where

$$\eta_1 \sim \eta_0 + \partial_z \eta + \frac{1}{2} \partial_z^2 \eta; \quad \partial_z \eta|_{z=1} \sim \partial_z \eta + \partial_z^2 \eta,$$

given

$$\eta_0 = (v_c^0/c)^2, \quad \partial_z \eta \sim 2v_c^0 \partial_z v_c \quad \text{and} \quad \partial_z^2 \eta \sim 2(\partial_z v_c)^2.$$

6. Error characterization

In this section, we show the comparison between analytically approximated and numerically computed results for $\kappa_{\nu\gamma}$ and $V_{\nu\gamma}$. We have explored the results for the t_{21} mode since this is sufficient for our purposes. We define the differences between analytically approximated ($\kappa_{\nu\gamma}^t$, $V_{\nu\gamma}^t$) and numerical ($\kappa_{\nu\gamma}^n$, $V_{\nu\gamma}^n$) results as follows:

$$R_\kappa = \left| \frac{\kappa_{\nu\gamma}^t - \kappa_{\nu\gamma}^n}{\kappa_{\nu\gamma}^t + \kappa_{\nu\gamma}^n} \right|, \quad (\text{A39})$$

$$R_V = \left| \frac{V_{\nu\gamma}^t - V_{\nu\gamma}^n}{V_{\nu\gamma}^t + V_{\nu\gamma}^n} \right|. \quad (\text{A40})$$

In Fig. 9, we plot the characteristics of R_κ and R_V for three cases, i.e., when $\partial_z v_c \in \{0, 10^{-3} cL^{-1}, -10^{-4} cL^{-1}\}$. The

³²Note that the occurrences of (g) in the expressions of $\mathcal{L}_3^{(g)}$, $\mathcal{L}_4^{(g)}$, and $\mathcal{L}_5^{(g)}$ are intended as superscripts and not exponents.

leftmost panels show a baseline mismatch between the approximated analytical values and the numerically calculated values of $\kappa_{\nu\gamma}$ and $V_{\nu\gamma}$. Note that, since $\partial_z v_c = 0$ for these two panels, the numerical and approximated analytic results should not have a significant mismatch. However, the results deviate from accuracy for certain regions in parameter space, especially for lower values of v_c^0 . The center and rightmost panels show similar characteristics. Note that the mismatch in $\kappa_{\nu\gamma}$ and $V_{\nu\gamma}$ follows somewhat similar characteristics to the time scales plotted in Fig. 4. The underlying reason is fairly straightforward: larger time scales occur when K_s becomes large in magnitude, and this large magnitude of K_s tends to make the numerical results less accurate, while the approximated analytic results continue to follow an accurate path. Note that the factor $\rho_e(z)$ in the expressions of $\kappa_{\nu\gamma}$ and $V_{\nu\gamma}$ tends to fall very rapidly with z from a large value ρ_0 at $z = 0$ for large magnitudes of K_s .³³ We also find that the numerical values of $Z_{\nu\gamma}(z)$ tend to wander inaccurately into the negative domain from tolerance-induced numerical errors nearing $z = 0$. This small discrepancy between the values calculated by numerical methods and approximate analytic expressions is amplified by the larger value of $\rho_e(z)$ nearing $z = 0$, especially when K_s is large, leading to a large mismatch. This effect also contributes to Fig. 9 in the case of $\partial_z v_c = 0$, i.e., the leftmost panels.

³³While this affects the numerical results of $\kappa_{\nu\gamma}$ and $V_{\nu\gamma}$, no such effect is present in the expression for the time scale $t_{\nu\gamma}$.

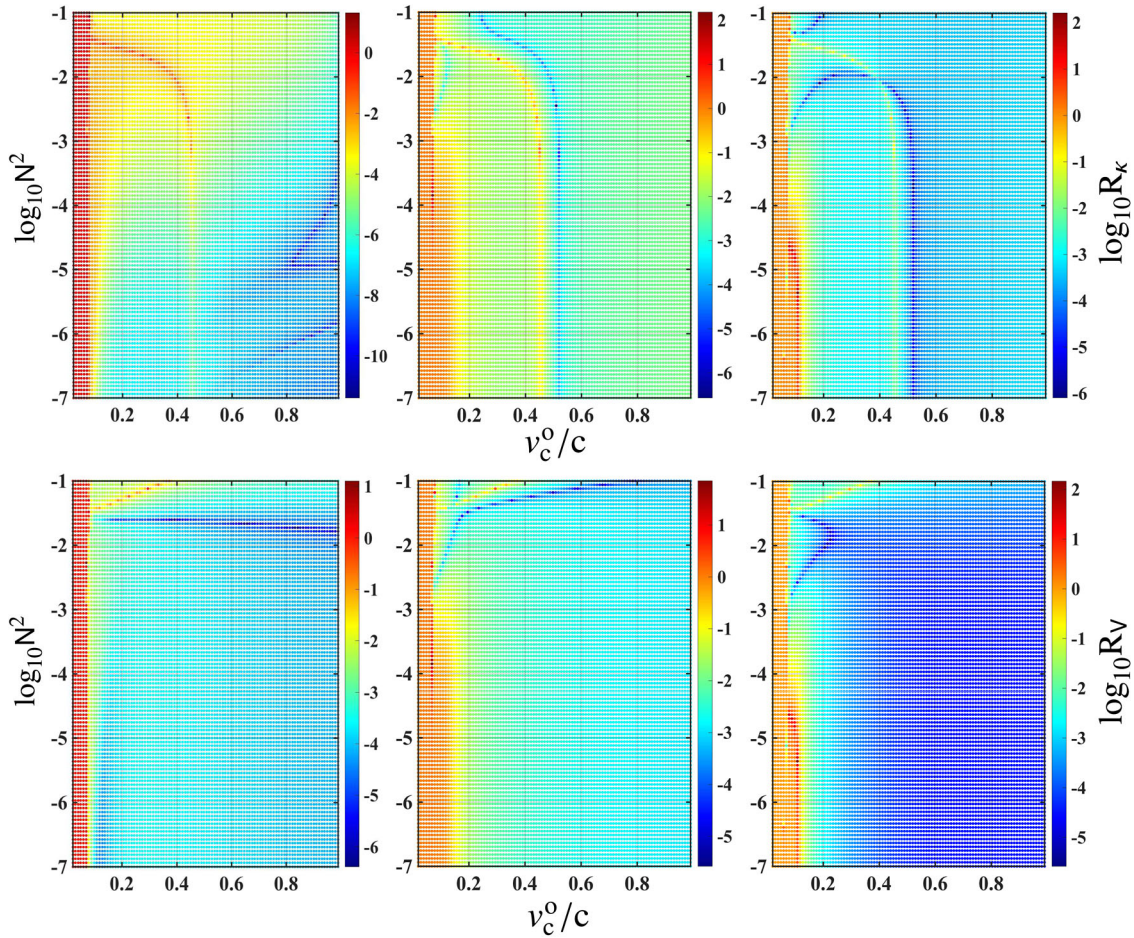


FIG. 9. Error characteristics. Three different sets of data are plotted for the t_{21} mode at a rotational frequency of 100 Hz, and for a set of values of $\partial_z v_c$: 0, $10^{-3} cL^{-1}$, and $-10^{-4} cL^{-1}$ (from left to right). Other relevant physical parameters are chosen from astrophysical priors, as in all of the previous figures. The top panel represents R_κ , while the bottom panel represents R_ν . Note that larger values of R_κ and R_ν signify a large mismatch between the approximated analytic and numerical results.

7. $t_{\nu\gamma}$ vs f

In this section, we elaborate on the characteristics of emitted signals as a function of a neutron star's rotational frequency f . In Fig. 10, we plot the time scales for the $\{2, 1\}$ and $\{1, 1\}$ modes, i.e., t_{21} and t_{11} , as a function of f . These time scales have been calculated and implicitly included in the results via (84) in Fig. 7. We can conclude from Fig. 10 that these time scales may span orders of magnitudes. For (84) to be a valid measure of minimum detectable strain for such signals, the observation time for the coherent search must be larger than these time scales, i.e., $T_{\text{obs}} \geq t_{\nu\gamma}$.

Moreover, there is a noticeable dip in emission from current-quadrupole contribution in the midfrequency range in Fig. 7. This dip is caused by $V_{\nu\gamma}$ becoming negative with increasing frequency. The sharp dip occurs due to the inclusion of $V_{\nu\gamma}$ in (72)–(75) via its absolute magnitude. This effect is not limited to the $V_{\nu\gamma}$ and current-quadrupole contribution only. In fact, the presence of this dip in

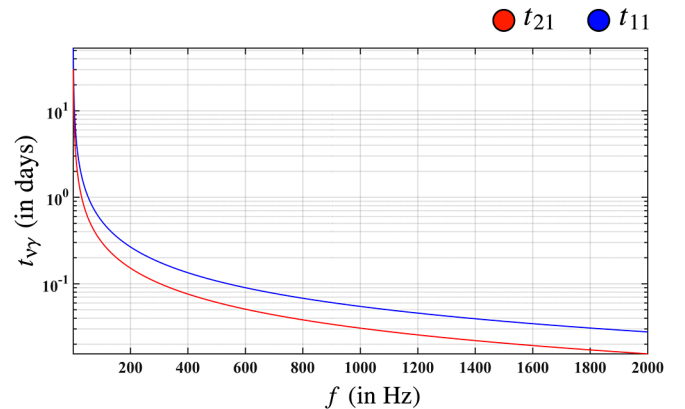


FIG. 10. $t_{\nu\gamma}$ characteristics. t_{21} and t_{11} are plotted as a function of a neutron star's rotational frequency f . We have set $v_c^0 = 0.1c$, $N^2 = 10^{-4}$, $E = 10^{-10}$, $\epsilon = 10^{-4}$, $d_s = 1$ kpc, $L = 10^4$ m, $g = 10^{12}$ m/sec², $\rho_o = 10^{17}$ kg/m³, $\partial_z v_c = 0$.

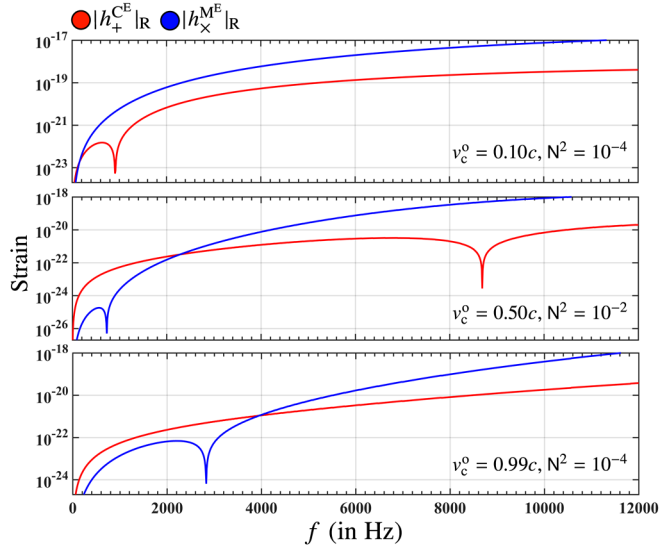


FIG. 11. Emission characteristics. We have set $E = 10^{-10}$, $\epsilon = 10^{-4}$, $d_s = 1$ kpc, $L = 10^4$ m, $g = 10^{12}$ m/sec², $\rho_o = 10^{17}$ kg/m³, $\partial_z v_c = 0$, and three different sets of values of v_c^0 and N^2 are explored. Note the appearance of dips in one or both of the contributions in frequency space, i.e., mass-quadrupole and current-quadrupole emissions, due to a variation in v_c^0 and N^2 .

current-quadrupole or mass-quadrupole emission depends upon the values of v_c^0 and N^2 . Like $V_{\nu\gamma}$, $\kappa_{\nu\gamma}$ may also show a similar effect for alternative values of v_c^0 and N^2 . Furthermore, the location of this dip in frequency space is found to vary with v_c^0 as well as N^2 . We also find that the location of this dip is less sensitive to variation in N^2 than in v_c^0 . In Fig. 11 above, we plot a part of Fig. 7 (the top-right panel) to demonstrate the aforementioned effect.

8. Dependence of emission properties on $\partial_z v_c$

The significant and critical affect of $\partial_z v_c$ on the properties of the gravitational wave emission discussed in Secs. V

and VI is best estimated by looking at (42) and the discussion in Sec. A of this appendix. For instance, (A2) equates the rate of flow into the viscous boundary layer at the top and bottom faces of the cylinder with the rate of flow out of this boundary layer back into the bulk; this is a direct consequence of the conservation of mass across the viscous boundary layer [5,15–17]. This rate of exchange of fluid determines the dissipation time scale of a certain perturbed $\{\alpha, \gamma\}$ mode—faster exchange of fluid leads to faster dissipation of the perturbation. The value of $\partial_z v_c$ bears a direct consequence on this process at the boundary layer. For example, from (A8) and (46), we see that $\partial_z v_c$ contributes via the “slope term” $\partial Z_{\alpha\gamma}/\partial z$, and the $\partial_z \eta$ term in the denominator in (A8). In fact, the $\partial Z_{\alpha\gamma}/\partial z$ term is the dominant determinant in deciding the speed of exchange since $|\partial_z \eta| \ll 1$. When the slope term is large and positive, the exchange of fluid is slow, as is clearly seen in (A8). This is simply because the fluid flowing out of the boundary layer and back into the bulk has to work against a high pressure gradient at $z = \pm 1$, which is set by the positive value of the slope term. Note that the positive slope of $Z_{\alpha\gamma}$ implies decreasing pressure in the z direction, as seen in (41). Similarly, when the slope term is positive but small, the exchange of fluid is faster since the pressure gradient decreases in value. Note that when the slope term becomes negative, we may see growing modes, although this is neither a sufficient nor a necessary condition; the growing modes could also occur when $N^2 < 0$ despite the slope being positive. This effect is seen in Fig. 4, where the value $\partial_z v_c = -10^{-4} cL^{-1}$ increases the characteristic time scales as well as the corresponding gravitational wave amplitudes in some regions of the parameter space. It is important to remember here that this increase in gravitational wave amplitude occurs at the resonance frequency only, and the amplitudes decay in the sidebands. Hence, while increasing time scales increase the gravitational wave amplitude at the resonance frequency, they also decrease the effective bandwidth of the signal frequency.

[1] S. Dall’Osso, G.L. Israel, L. Stella, A. Possenti, and E. Perozzi, The glitches of the anomalous x-ray pulsar 1RXS J170849.0-400910, *Astrophys. J.* **599**, 485 (2003).
 [2] A. G. Lyne, S. L. Shemar, and F. Graham Smith, Statistical studies of pulsar glitches, *Mon. Not. R. Astron. Soc.* **315**, 534 (2000).
 [3] M. Yu, R. N. Manchester, G. Hobbs, S. Johnston, V. M. Kaspi, M. Keith, A. G. Lyne, G. J. Qiao, V. Ravi, J. M. Sarkissian, R. Shannon, and R. X. Xu, Detection of 107 glitches in 36 southern pulsars, *Mon. Not. R. Astron. Soc.* **429**, 688 (2013).

[4] A. Melatos, C. Peralta, and J. S. B. Wyithe, Avalanche dynamics of radio pulsar glitches, *Astrophys. J.* **672**, 1103 (2008).
 [5] C. A. van Eysden and A. Melatos, Searches for periodic gravitational waves from unknown isolated sources and Scorpius X-1: Results from the second LIGO science run, *Classical Quantum Gravity* **25**, 225020 (2008).
 [6] N. Andersson, G. L. Comer, and R. Prix, Are Pulsar Glitches Triggered by a Superfluid Two-Stream Instability?, *Phys. Rev. Lett.* **90**, 091101 (2003).
 [7] A. Mastrano and A. Melatos, Kelvin-Helmholtz instability and circulation transfer at an isotropic-anisotropic

- superfluid interface in a neutron star, *Mon. Not. R. Astron. Soc.* **361**, 927 (2005).
- [8] D. I. Jones and N. Andersson, Gravitational waves from freely precessing neutron stars, *Mon. Not. R. Astron. Soc.* **331**, 203 (2002).
- [9] C. Peralta, A. Melatos, M. Giacobello, and A. Ooi, Global three-dimensional flow of a neutron superfluid in a spherical shell in a neutron star, *Astrophys. J.* **635**, 1224 (2005).
- [10] I. Easson, Postglitch behavior of the plasma inside neutron stars, *Astrophys. J.* **228**, 257 (1979).
- [11] V. Rezanian and M. Jahan-Miri, The possible role of r -modes in post-glitch relaxation of the Crab pulsar, *Mon. Not. R. Astron. Soc.* **315**, 263 (2000).
- [12] D. M. Sedrakian, M. Benacquista, K. M. Shahabassian, A. A. Sadoyan, and M. Hairapetyan, Gravitational radiation from fluctuations in rotating neutron stars, *Astrophysics* **46**, 445 (2003).
- [13] D. M. Sedrakian, M. Benacquista, and K. M. Shahabassian, Gravitational radiation of slowly rotating neutron stars, *Astrophysics* **49**, 194 (2006).
- [14] N. Andersson, T. Sidery, and G. L. Comer, Mutual friction in superfluid neutron stars, *Mon. Not. R. Astron. Soc.* **368**, 162 (2006).
- [15] M. F. Bennett, C. A. van Eysden, and A. Melatos, Continuous-wave gravitational radiation from pulsar glitch recovery, *Mon. Not. R. Astron. Soc.* **409**, 1705 (2010).
- [16] G. Walin, Some aspects of time-dependent motion of a stratified rotating fluid, *J. Fluid Mech.* **36**, 289 (1969).
- [17] M. Abney and R. I. Epstein, Ekman pumping in compact astrophysical bodies, *J. Fluid Mech.* **312**, 327 (1996).
- [18] P. M. McCulloch, P. A. Hamilton, D. McConnell, and E. A. King, The Vela glitch of Christmas 1988, *Nature (London)* **346**, 822 (1990).
- [19] C. A. van Eysden and A. Melatos, Gravitational radiation from pulsar glitches, *J. Fluid Mech.* **729**, 180 (2013).
- [20] J. Mound and B. Buffett, Viscosity of the Earth's fluid core and torsional oscillations, *J. Geophys. Res. Solid Earth* **112**, B05402 (2007).
- [21] A. Adare *et al.*, J/ψ Production versus Centrality, Transverse Momentum, and Rapidity in Au + Au Collisions at $\sqrt{s_{NN}} = 200$ GeV, *Phys. Rev. Lett.* **98**, 172301 (2007).
- [22] S. S. Adler *et al.*, Elliptic Flow of Identified Hadrons in Au + Au Collisions at $\sqrt{s_{NN}} = 200$ GeV, *Phys. Rev. Lett.* **91**, 182301 (2003).
- [23] P. K. Kovtun, D. T. Son, and A. O. Starinets, Viscosity in Strongly Interacting Quantum Field Theories from Black Hole Physics, *Phys. Rev. Lett.* **94**, 111601 (2005).
- [24] D. Mateos, R. C. Myers, and R. M. Thomson, Holographic Viscosity of Fundamental Matter, *Phys. Rev. Lett.* **98**, 101601 (2007).
- [25] C. Cutler and L. Lindblom, The effect of viscosity on neutron star oscillations, *Astrophys. J.* **314**, 234 (1987).
- [26] A. Melatos and C. Peralta, Superfluid turbulence and pulsar glitch statistics, *Astrophys. J.* **662**, L99 (2007).
- [27] K. S. Thorne, Multipole expansions of gravitational radiation, *Rev. Mod. Phys.* **52**, 299 (1980).
- [28] A. Melatos and C. Peralta, Gravitational radiation from hydrodynamic turbulence in a differentially rotating neutron star, *Astrophys. J.* **709**, 77 (2010).
- [29] See J. R. Holton, *An Introduction to Dynamic Meteorology* (Academic, New York, 1972); J. Lighthill, *Waves in Fluids* (Cambridge University Press, Cambridge, England, 2000).
- [30] N. Andersson, G. L. Comer, and K. Glampedakis, How viscous is a superfluid neutron star core?, *Nucl. Phys. A* **763**, 212 (2005).
- [31] J. L. Friedman and N. Stergioulas, *Rotating Relativistic Stars* (Cambridge University Press, Cambridge, England, 2013).
- [32] M. van Hoven and Y. Levin, On the excitation of f -modes and torsional modes by magnetar giant flares, *Mon. Not. R. Astron. Soc.* **410**, 1036 (2011).
- [33] B. Abbott *et al.*, Searches for periodic gravitational waves from unknown isolated sources and Scorpius X-1: Results from the second LIGO science run, *Phys. Rev. D* **76**, 082001 (2007).
- [34] D. Keitel, Robust semicoherent searches for continuous gravitational waves with noise and signal models including hours to days long transients, *Phys. Rev. D* **93**, 084024 (2016).
- [35] R. Prix, S. Giampanis, and C. Messenger, Search method for long-duration gravitational-wave transients from neutron stars, *Phys. Rev. D* **84**, 023007 (2011).
- [36] M. Abney, R. I. Epstein, and A. V. Olinto, Observational constraints on the internal structure and dynamics of the Vela pulsar, *Astrophys. J.* **466**, L91 (1996).
- [37] C. A. van Eysden, Short-period pulsar oscillations following a glitch, *Astrophys. J.* **789**, 142 (2014).